INL/EXT-21-62688

Evaluation of Two-Dimensional to One-Dimensional Site Response at Idaho National Laboratory

April 2021

INL/EXT-21-62688

Evaluation of Two-Dimensional to One-Dimensional Site Response for Idaho National Laboratory

Domniki Asimaki
California Institute of Technology
Pasadena, California

April 2021

Idaho National Laboratory
Idaho Falls, Idaho 83415

http://www.inl.gov

Prepared for the
U.S. Department of Energy
Office of Nuclear Energy
Under DOE Idaho Operations Office
Contract DE-AC07-05ID14517

SUMMARY

We perform two-dimensional (2D) site response analyses accounting for spatial variability of soil properties and subsurface geometry of the Eastern Snake River Plane (ESRP), and quantify their effects on ground surface motion relative to one-dimensional (1D) site response analyses at the Idaho National Laboratory (INL). We first present the development of random field idealizations of the repeated basalt lava flows, heterogeneously inter-layered with sediments, from seismic velocity data collected over four decades in the ESRP. Using realizations of the stochastic fields mapped on 2D deterministic finite element models, we perform 2D viscoelastic and equivalent-linear wave propagation simulations, and quantify the mean and variance of site response aggravation factors, defined as the response spectral ratio of 2D to 1D analyses on the ground surface. Results are shown to be insensitive to the constitutive material behavior considered here, for strains induced by rock outcrop peak ground acceleration (PGA) as high as 0.7g: viscoelastic and equivalent-linear analyses predict peak mean 2D/1D aggravation factor 1.05 at period T=0.075 sec (i.e. the 2D response spectrum is 5% higher than the corresponding 1D at that period, on average), which corresponds to the wavelength of the horizontal correlation length of the random field (50m). For periods longer than the fundamental period of the site (here, T_1=0.3125 sec), the propagating wavelengths are too long to be affected by the 1D site response and the aggravation factor becomes equal to 1. The standard deviation of the natural logarithms of the 2D/1D aggravation factors is ~0.15 for periods shorter than the fundamental period of the site, and decays thereafter at a steady rate.

Next, we present results from 2D site response analyses in the vicinity of proposed Carbon Free Power Project (CFPP) referred to as Site 3 (also USGS Borehole 142) in the ESRP, which is characterized by a wedge-like subsurface geometry likely to generate focusing effects and significant surface wave amplification. We perform vertically propagating plane wave analyses, and inclined plane wave analyses for a range of incidence angles (45º, 55 º, and 75º) informed by the Seismic Source Characterization (SSC) logic tree parameters for the Big Lost River fault dip. Both horizontal and vertical ground surface motions are normalized by the corresponding 1D ground response predictions. Vertical and inclined plane wave analyses show that the 2D/1D aggravation factor of the horizontal component, generated by

diffraction near the edge, is larger than 1.0 for periods T<1.2 sec. Vertically propagating waves yield 2D/1D aggravation ~1.8 in a very narrow zone near Site 3, whereas inclined waves yield lower aggravation of the horizontal component (<1.5) over a wider zone consistent with stronger generated surface waves propagating away from the edge. The vertical component that is not accounted for in 1D site response analyses reaches spectral amplitudes nearly as large as the horizontal spectral acceleration that would have been predicted from 1D ground response analyses within 5-10 km from the edge. This finding is relevant to the vertical to horizontal (V/H) factors that will be used to estimate vertical ground motion amplitude from 1D horizontal site response analyses near Site 3. In light of the idealized, sharp corner geometry that we use to model edge effects, results should be interpreted in the context of wavelength filtering: a narrow band of high frequencies is expected to be affected by the sharp corners, yet the effect is of a very narrow band nature, and using a moving averaging window across the model should smooth away associated biases. Better subsurface geometry and stratigraphy, more realistic source models, and three-dimensional (3D) wave propagation simulations should be considered to improve the accuracy of our 2D/1D aggravation factor estimations.

Evaluation of Two-Dimensional to One-Dimensional Site Response at the Idaho National Laboratory

Prepared under contract NO. 230555, BATTELLE ENERGY ALLIANCE, LLC (BEA)
(in accordance with the Statement of Work SOW-16899)

Domniki Asimaki
domniki@caltech.edu

April 19, 2021

Contents

1 Introduction

The Idaho National Laboratory is located in the Eastern Snake River Plain (ESRP), a broad low-relief basin floored with basaltic lava flows representing the northeast-trending track of the Yellowstone hotspot. ESRP has subsided and filled with up to 1.9 km of basalt lava flows and sediments to produce a complex subsurface of repeated basalt lava flows heterogeneously inter-layered with sediments. At the Idaho National Laboratory, sediments are derived from mainstream alluvium along the Big Lost River and, away from the river, from windblown sediments and localized drainages. During periods of basaltic volcanic activity sequences of multiple lava flows several tens to hundreds of meters thick accumulated and in intervening periods, sediments accumulated to thicknesses ranging from centimeters to tens of meters. Facility locations have both vertical and lateral variations of subsurface strata that require challenging approaches to ground motion modeling.

In this report, we examine how the spatial variability of soil properties and subsurface geometry of ESRP challenge the assumptions of 1D site response analyses that will be used to characterize ground motion seismic hazard at the Idaho National Laboratory. The report is organized as follows: Section 2 summarizes the development of random field idealizations of the repeated basalt lava flows heterogeneously inter-layered with sediments from seismic velocity data collected over four decades at ESRP; Section 3 outlines the numerical platform that we used for the two-dimensional wave propagation simulations; Section 4 presents the summary of our two-dimensional site response analyses for the viscoelastic and equivalent linear wave propagation simulations through the basalt lava-sediment random fields; and Section 5 presents 2D site response analyses to vertical and inclined plane wave incidence in the vicinity of Site 3 (also USGS Borehole 142) in the ESRP, which is characterized by a wedge-like subsurface geometry and is expected to generate significant refraction and focusing effects.

2 Random Fields: Basalt and Sedimentary Interbeds

Soil properties in a homogeneous soil layer are affected by a series of uncertainties, such as inherent spatial variability, random test errors, systematic test errors (or bias), transformation uncertainty (from index to design soil properties) etc. Since deterministic descriptions of this spatial variability are in general not feasible, the overall characteristics of the spatial variability and the uncertainties involved are mathematically modeled using stochastic (or random) fields. In this study, we used shear wave velocity measurements from the basalt-sediment interbed deposits to develop univariate stochastic fields describing the variability of a single soil property over the spatial domain of interest. For the statistical correlation between field values at different spatial locations, the statistics of spatial variability of soil properties need to be estimated, which refer to the average values (or spatial trends), the standard deviation, the (cross-) correlation structure, and the probability distribution functions.

To derive two-dimensional random field statistics for the basalt-sediment interbeds formation, we first identified seismic velocity data of the appropriate lithology with resolution adequate to capture the spatial statistics of the vertical and horizontal correlation lengths of the interbeds. [1] summarized thirty sets of seismic velocity data collected over the course of four decades using seven different seismic methods at the four facility areas and in regional boreholes. Many of the shear-wave velocity measurements were in the top 10 m of the interbedded basalt-sediment sequence with the exception of one borehole, which has shear-wave velocities to a depth of 350 m. For the purposes of this study, we used shear wave velocity measurements at sites ANL, INTEC and NRF (Figure 1). Profiles at these sites were selected from the VelocityData All-INL-sites.xls spreadsheet. For each borehole, the values of seismic velocity (shear, V_s, or compressional, Vp), depth, and lithology are provided for each layer. Additional information was extracted, where necessary, from Tables in [1] and tabs of the spreadsheet.

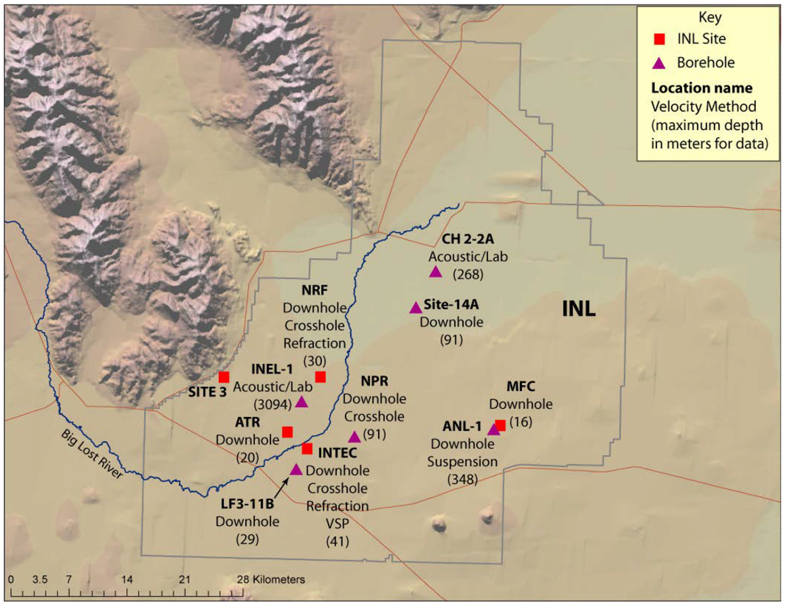

Figure 1: From [1], illustrating the locations of facility and available V_p and V_s data along with the methods used. Parentheses list the maximum depth of velocity data (in meters) at that location for all methods.

To evaluate the effects of stochastic distribution of soil properties on the response spectral amplification of the ground surface relative to the one dimensional site response, we used the Monte Carlo method: digital simulations of stochastic fields were combined with deterministic finite element analyses, while the material properties over the spatial domain of interest were modeled as a univariate (here, V_s), multi-dimensional, non-Gaussian stochastic field. Adopted from [2], the Monte Carlo procedure involves four basic steps:

i Estimation of the statistics of spatial variability (spatial trends, spatially dependent variance, probability distribution functions, correlation structure) based on the field measurement program,

ii Digital generation of sample functions of a two-dimensional, non-Gaussian stochastic field, each simulated sample function representing a possible realisation of soil property values over the analysis domain,

iii Evaluation of soil constitutive model parameters at every spatial location (finite element centroids) using correlations with in situ soil test results, and

iv Deterministic finite element analyses using stochastic parameter input derived from each sample field of soil properties; a sufficient number of finite element simulations has to be performed to derive the statistics of the response.

2.1 Parameter Estimation of Stochastic Fields

For the field data analysis, heterogeneous V_s measurements (crosshole, downhole, suspension logging) were initially combined and resampled every 0.5m (Figure 2). The spatially homogenized V_s measurements were successively averaged over a moving window of 2m (four resampled points per window); the latter was later evaluated by comparison with the correlation length in the vertical direction. This final smoothed V_s dataset was thereafter used to evaluate the spatial statistics in the vertical direction; mean and coefficient of variation (COV) thereof are shown in (Figure 3). Shear wave velocity was anticipated to be influenced by confining stress, so trends were expected in the vertical direction. The vertical data non-stationarity was evaluated within the *statistically homogenous* basalt-sediment interbed deposit as follows:

i The values $V_s(z) = V_s$ were expressed as sums of spatial trends –average and residuals (or fluctuations about spatial trends)– where z represents the spatial location (depth). The residuals were further normalized by the sample standard deviation of the field data to derive zero-mean, unit-variance homogeneous shear wave velocity fields. The trend in the vertical direction $(V_s - av(z))$ that was obtained by means of linear regression analysis is shown as a dashed line in Figure 4 (left).

ii Recognizing that the strongly fluctuating nature of the sample COV (Figure 3 right) is, at least in part, the result of the limited number of samples available to derive stable spatial statistics, a COV trend was identified using linear regression (dashed line in Figure 4 right); this bilinear COV was successively used to compute a smoothed standard deviation from the smoothed $Vs(z)$, which was next used to estimate the standardized (zero-mean, unit-variance) shear wave velocity profile values shown below.

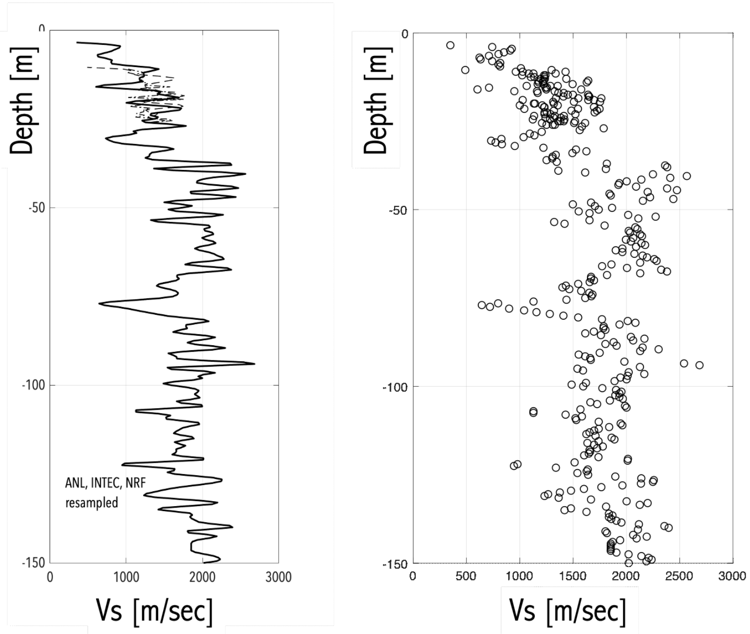

Figure 2: V_s measurements (left) and resampled V_s data ensemble (right; 0.5m interval) used in the estimation of the basalt-sediment interbed statistics.

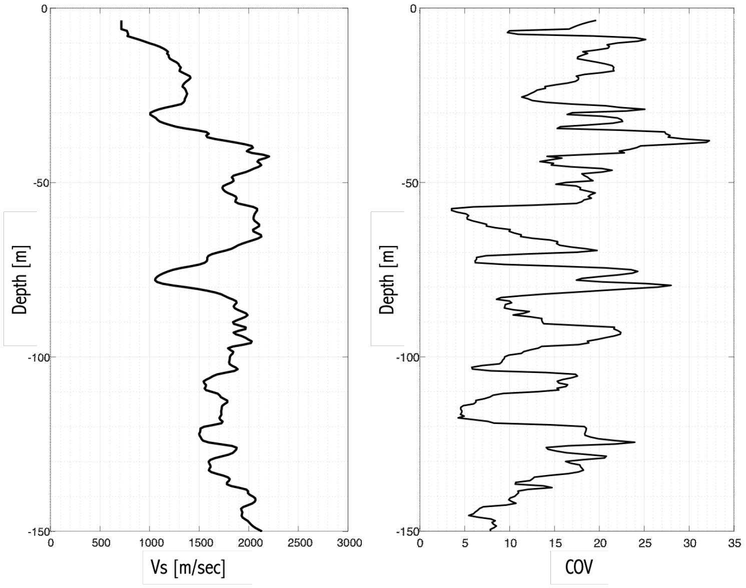

Figure 3: Moving average and COV estimation of the V_s data ensemble variation with depth.

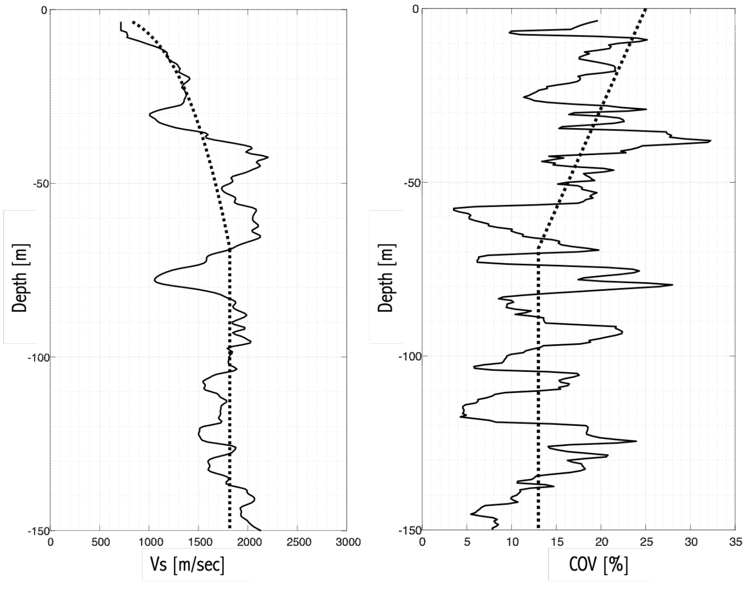

Figure 4: Estimation of background medium trends, $V_s - av(z)$ and COV with depth, used to computed the standardized datasets.

The best fit to the empirical probability distribution function of the standardized data histogram shown in Figure 5 was found to be the extreme value type I distribution for the smallest extreme; the extreme value type I distribution is also referred to as the Gumbel distribution, and has the following analytical probability distribution function:

$$f(x) = \frac{1}{\beta} e^{\frac{x-\mu}{\beta}} e^{-e^{\frac{x-\mu}{\beta}}} \tag{1}$$

where μ is the location parameter and β the scale parameter. For the digital generation of the stochastic fields, we further truncated the lower extreme of the distribution to $[-2\sigma, 2\sigma]$.

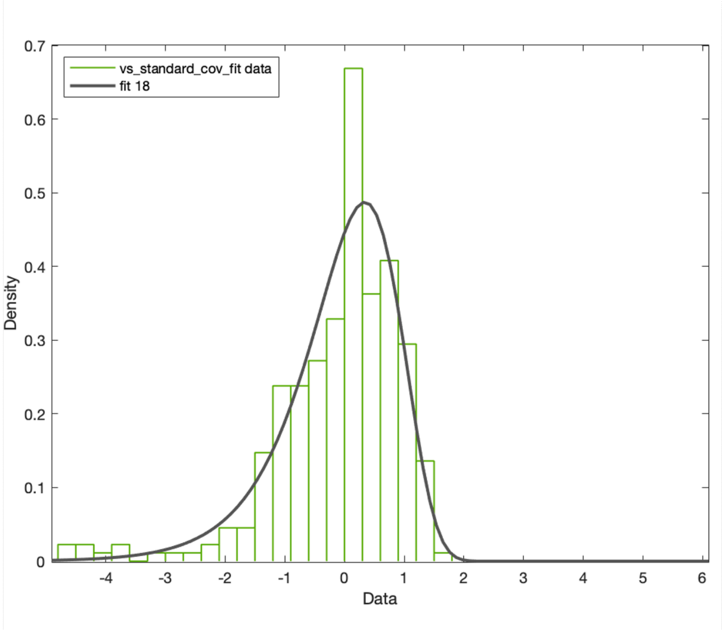

Figure 5: Empirical V_s standardized histogram and least-square fit of the extreme value type I distribution for the smallest extreme (Gumbel type I).

The mechanisms of soil formation in the horizontal and vertical directions are different enough that separable correlation structure models seem appropriate to simulate spatial variability of soil properties [3]. To capture the vertical spatial correlation, we used the decaying correlation structure below (s_{ED} in Equation (2)), which is derived from the Exponential Decaying spectral density function and discussed among others by [4]. The corresponding correlation function ρ_{ED} also shown below was presented in [2]:

$$\begin{aligned} s_{\mathrm{ED}}(\kappa) &= \tfrac{1}{2\Gamma(b_2+1)} b_1^{b_2+1} \kappa^{b_2} e^{-b_1|\kappa|}, b_1, b_2 > 0 \\ \rho_{\mathrm{ED}}(\xi) &= 2\int_0^\infty s(\kappa)\cos(\kappa\xi)d\kappa = \frac{\cos\left[(b_2+1)\tan^{-1}\left(\frac{\xi}{b_1}\right)\right]}{\left[1+\left(\frac{\xi}{b_1}\right)^2\right]^{\frac{b_2+1}{2}}}. \end{aligned} \tag{2}$$

We specifically implemented a more versatile form of the exponential decaying function originally proposed by [2] that is formulated as a sum of two Exponential Decaying spectral density functions (Equation (3)); the autocorrelation function is shown in Figure 6. The vertical correlation length was estimated from Equation (4) to be approximately $\theta_z = 9$m.

$$\rho_{\mathrm{TP}}\left(\xi, b_1, b_2, b_3, b_4, b_5\right)=b_5 \rho_{\mathrm{ED}}\left(\xi, b_1, b_2\right)+\left(1-b_5\right) \rho_{\mathrm{ED}}\left(\xi, b_3, b_4\right) \tag{3}$$

$$\theta=\int_0^{\xi_1} \rho(\xi) d \xi, \quad \xi_i=b_1 \tan \frac{\pi}{2\left(b_2+1\right)} \tag{4}$$

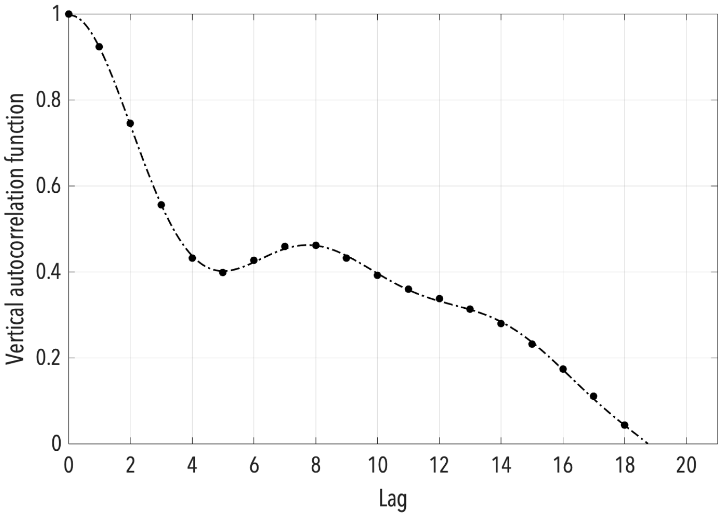

Figure 6: Vertical autocorrelation function of standardized V_s data ensemble.

For the horizontal correlation structure, we first assumed a radial correlation structure (that is independent of the direction in a plane); this allowed us to use data from all boreholes, projected on a plane across the site, as shown in Figure 7. However, the limited availability of closely spaced borehole data in the horizontal direction yielded non-significant correlations between V_s profiles. We thus resorted to using a simple exponential model for the theoretical correlation function in the horizontal direction as shown in Equation (5).

$$\rho\left(\xi_x\right)=\exp \left(-\frac{2 \xi_x}{b_1}\right) \tag{5}$$

The correlation length, θ_x, was estimated as a function of the vertical correlation length $\theta_z = 9$m as described in [5] and [6], namely $\theta_x \approx 5 - 10 \times \theta_z = 50 - 100$m. We evaluated the sensitivity of our findings to the choice of horizontal correlation length by generating both $\theta_z = 50$m and $\theta_z = 100$m digital random fields as described below, and computing the 2D site response of each ensemble. Results are presented in Section 3 of this report.

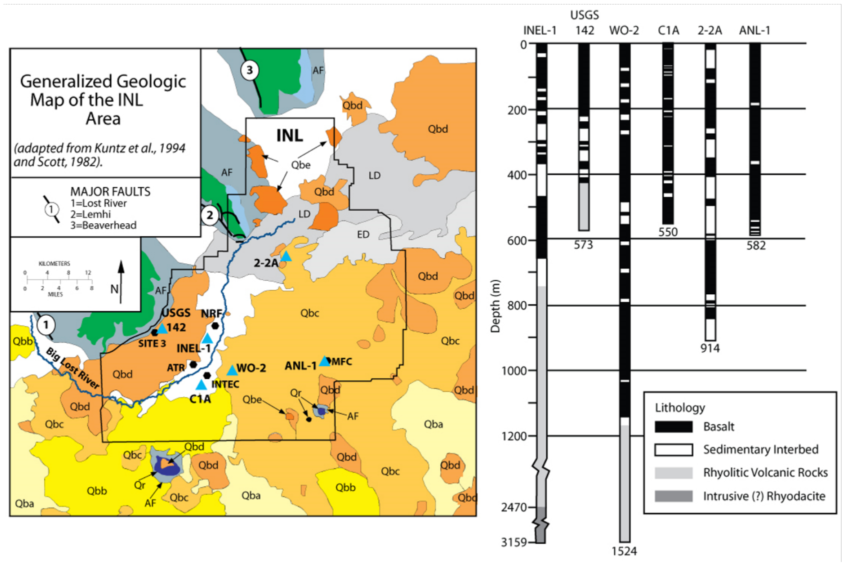

Figure 7: (left) Geologic map of the INL (adapted from Scott 1982; Kuntz et al. 1994) and boundaries of three volcanic rift zones (A – Arco, H – Howe-East Butte, and L – Lava Ridge-Hell's Half Acre) and Axial Volcanic Zone (AVZ). Facility areas (black hexagons), Advanced Test Reactor (ATR), Idaho Nuclear Technology and Engineering Center (INTEC), and Naval Reactor Facility (NRF), are located in mainstream alluvium of the Big Lost River. The Materials and Fuels Complex (MFC) is located on basalt lava flows covered by a few meters of eolian sand and loess (from [1]); (right) Summary of the lithology of boreholes INEL-1, USGS142, WO-2, CH2-2A, and ANL-1 (from Payne 2019).

Lastly, we should point out that we did investigate cross-correlation structures between the measured V_s profiles used to derive the field statistics, and other material property measurements available at the same locations, such as density (ρ). No statistically significant correlation was identified between the V_s and ρ, which led us to pursue the generation of two sets of single variate (V_s, ρ), two-dimensional (2D) random fields instead of one cross-correlated bi-variate 2D set of random fields. Furthermore, there was no significant trend of the background density medium with depth (as shown on the left hand side of Figure 8) and the standardized empirical density histogram shown on the right hand side of Figure 8 was fit with a simple Gaussian distribution. The latter, truncated between $[-2\sigma, 2\sigma]$ in accordance with the V_s probability distribution function described above, was used to sample ρ random fields for every V_s random field realization. There were not enough data for us to estimate the field statistics of Poisson's ratio, which was assumed constant throughout the computational domain and equal to $\nu = 0.35$ following [1].

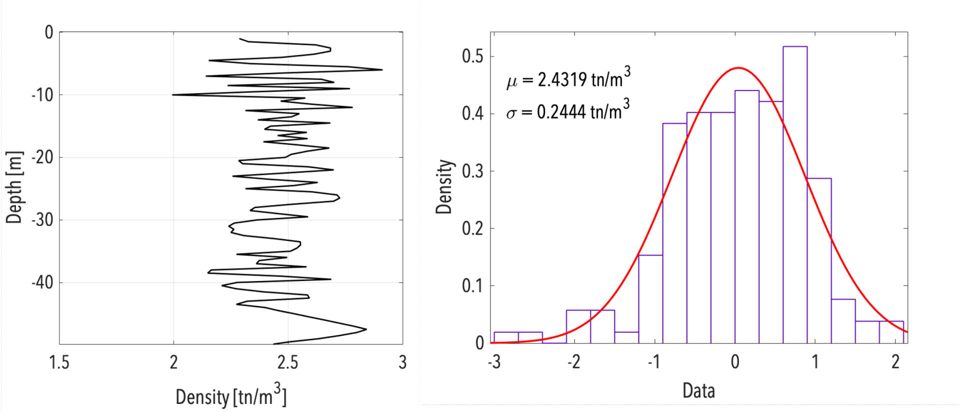

Figure 8: Variation of empirical density data with depth (left) and standardized empirical density histogram (right), along with the least-square best fit of a Gaussian distribution and corresponding parameters (μ, σ). The latter, truncated between $[-2\sigma, 2\sigma]$, was used to sample ρ random fields for every V_s random field realization

2.2 Simulation of Stochastic Fields

Following the methodology described by [2], one hundred (100) sample functions of single variate (V_s), two-dimensional (2D) random fields were generated to ensure convergence of the field and wave propagation statistics during the second step of the Monte Carlo simulation procedure described above. Successively, a mapping technique was necessary to transform the sample fields (where the random variables are evaluated at predetermined spatial locations) to the finite element mesh for the deterministic analyses that followed (e.g. [7]). Note that the mesh size for stochastic field generation (here, required to depict with acceptable resolution the horizontal and vertical correlation lengths) is dictated by criteria that may be different from the finite element mesh (here, the need to propagate, without alias, the highest frequency through the softest layers of the material). Due to the incompatibility of the criteria, a mapping technique referred to as “the midpoint method” was employed, according to which the random field is represented by its values at the centroids of the finite elements prior to the estimation of the soil constitutive parameters needed for the deterministic equivalent linear analyses.

Figure 9 shows two realizations of the V_s stochastic fields with $\theta_z = 9$m and $\theta_x = 50$m (a) and $\theta_x = 100$m (b). The V_s stochastic fields are here mapped on a finite element mesh of element size $1 \times 1m^2$ allowing reliable energy propagation up to 20Hz. More information on the finite element analyses is provided below.

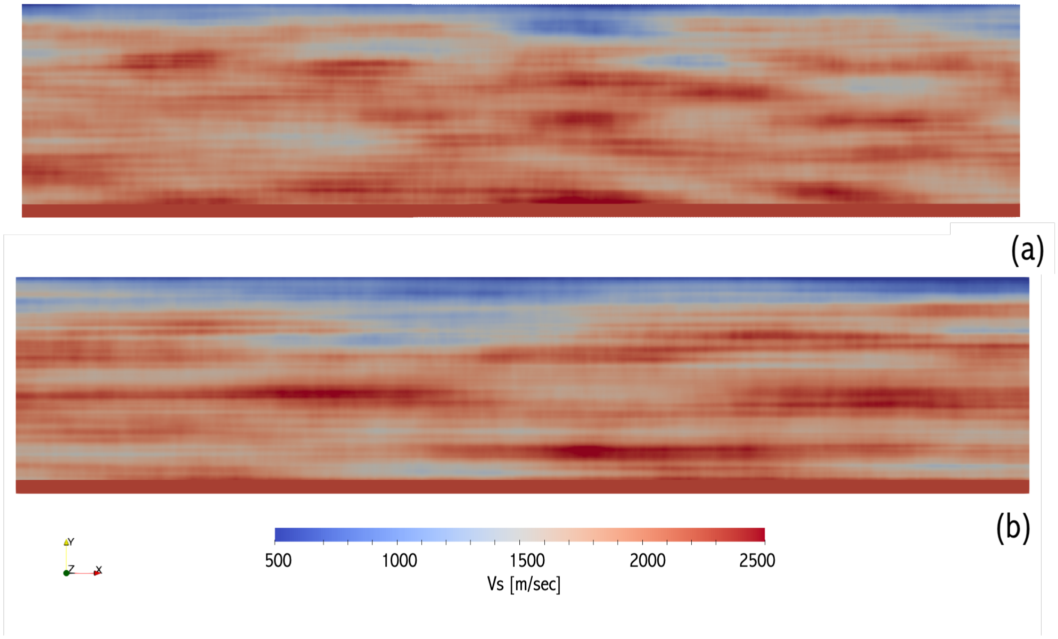

Figure 9: V_s stochastic fields with $\theta_z = 9$m and $\theta_x = 50$m (a) and $\theta_x = 100$m (b) mapped onto a structured, uniform 750m x 120m finite element mesh with element size $1 \times 1m^2$.

3 Finite Element Analyses: Overview of Seismo-VLAB

Finite element analyses were conducted using `Seismo-VLAB`, an open-source finite element code soon to be released that is being developed at Caltech. `Seismo-VLAB` [1] is a simple, fast, and extendable C++ [8] multi-platform code designed to optimize meso-scale (sub-km) finite element simulations. The code implements state-of-the-art tools to achieve optimal robustness and efficiency for wave-propagation problems. The most important features of the software include dynamic nonlinear solvers for time-domain analyses of inelastic problems; cutting-edge direct and iterative parallel linear system solvers; interfaces with Message Passing Interface (MPI) [9] and Open Multi-Processing (OpenMP) [10] parallelization; domain decomposition for optimal parallel computing [11]; perfectly matched layers as robust absorbing boundaries [12, 13]; domain reduction for modeling wave-field incoherency in truncated domains [14]; time-variant and time-invariant equivalent linear analyses; and a number of soil and structural plasticity models.

3.1 Domain Decomposition and Parallel Computing

Domain decomposition in `Seismo-VLAB` is carried out using Metis software [11]. Here, the model domain (i.e., group of objects such as `Node`, `Element`, `Material`, `Section`, and `Load`) is

---

[1] `www.seismovlab.com`

divided so that the number of elements are uniformly distributed across processors.

3.2 Absorbing Boundary Conditions

`Seismo-VLAB` employs perfectly Matched Layers (PML) to emulate the reflection-free boundary conditions of semi-infinite half-spaces in 2D [15, 12] and 3D [12, 13]. Currently, quadrilateral `PML2DQuad4` of four and `PML2DQuad8` of eight nodes are available in 2D, while hexahedral `PML3DHexa8` of eight and `PML3DHexa20` twenty nodes are implemented in 3D. The PML elements developed in `Seismo-VLAB` correspond to a fully-mixed symmetric formulation for both plane-strain (2D) and three-dimensional (3D) problems. We here briefly demonstrate the `Seismo-VLAB` PML implementation in 2D. Consider a truncated soil domain with dimensions $L_x = 150\,[m]$ (width) and vertical length $L_z = 100\,[m]$ (height). An isotropic linear elastic material for the soil is employed such that $\rho_s = 2000\,[kg/m^3]$, $\nu_s = 0.25$, $t_h = 1.0\,[m]$, and plane-strain conditions are enforced. In addition, a PML zone of $25\,[m]$ thickness is provided along the truncated domain. The model is subjected to a downward point load force, located at the middle of the surface. The force $F(t)$ is prescribed as an effective force Ricker function, proportional to Equation (6):

$$F(t) = \left(1 - 2\,(\pi\,\mathrm{f}_0)^2\,(t - t_0)^2\right) \exp\left[-(\pi\,\mathrm{f}_0)^2\,(t - t_0)^2\right] . \tag{6}$$

In this numerical example, we have employed a central frequency $\mathrm{f}_0 = 2.0\,[Hz]$, and the soil's shear wave velocity is set to be $V_s = 100\,[m/s]$. The finite element model has 1718 nodes, 61 restrains, 162 constraints, and 1578 elements divided as 980 `lin2DQuad4` and 580 `PML2DQuad4`. The simulation time is set to be $t_{\mathrm{sim}} = 10.0\,[s]$, with a temporal discretization of $\Delta t = 0.010\,[s]$, that is with $n_t = 1000$ time steps. In Figure 10 the velocity field amplitudes at (a) $t = 1.65\,[s]$, (b) $t = 2.25\,[s]$, and (c) $t = 3.00\,[s]$ are shown for the truncated soil domain. No reflections are generated from the PML boundaries. Using PML boundary conditions was particularly important for the site response simulations at INL, since the far field and base boundaries of the 2D numerical domain have properties randomly change each time a new realization is sampled from the V_s field statistics. A Python script was developed as part of this project to automatically generate compatible boundary conditions between the finite element mesh and the corresponding PML boundary elements.

Figure 10: A snapshot of velocity amplitude field in 2D under vertical loading at the surface of the domain.

3.3 Domain Reduction Method

`Seismo-VLAB` employs the domain reduction method (DRM) [14, 16] for modeling purposes of inclined plane waves and generic incoherent wave-fields in 2D and 3D. In order to maintain the DRM formulation as general as possible, the displacement, velocity and acceleration wave-fields are required to be specified over a single layer of finite elements. This information is then used internally to compute the effective force vector (that acts within that layer of elements) required to transmit the ground motion inside the DRM.

The DRM implementation in `Seismo-VLAB` is demonstrated with a simple example below. Consider a soil domain with dimensions $L_x = 150\,[m]$ (width) and $L_z = 100\,[m]$ (height). An isotropic linear elastic material for the soil is employed such that $\rho_s = 2000\,[kg/m^3]$, $\nu_s = 0.25$, $t_h = 1.0\,[m]$, and plane-strain conditions are enforced. The DRM is employed to capture the propagation of an in-plane SV-wave propagating at 15° angle. The incident ground motion is prescribed as a Ricker function similar to Equation (6). In this numerical example, we have employed a central frequency $\mathrm{f}_0 = 2.0\,[Hz]$, and $V_s = 50\,[m/s]$. The finite element model has 46202 nodes, 701 restrains, and 16402 elements divided into 15000 `lin2DQuad8` and 1402 `ZeroLength1D`, placed along the boundary to absorb the scattered wavefield. Figure 11 depicts the velocity field amplitude at (a) $t = 1.500\,[s]$, (b) $t = 2.1875\,[s]$, and (c) $t = 2.8125\,[s]$, where it can be readily seen that the excitation –comprising inclined SV-wave propagating at an 15° angle– is confined to the interior of the DRM elements. Using DRM input time series was important for the simulation of edge effects in the vicinity of Site 3 at INL, results of which are outlined in Section 4 of this report.

Figure 11: Snapshots of the 2D velocity amplitude field computed using the DRM load modeling for an inclined wave at incident angle of 15° degrees in a homogeneous half-space.

3.4 Nonlinearity: Equivalent Linear Analyses

`Seismo-VLAB` can accomodate problems involving large deformations, non-linear material behavior or both. Non-linear material laws are provided in a few material classes, including bounding surface multi-axial plasticity in `PlasticPlaneStrainBA`, and `Plastic3DBA` for clay modeling in 2D and 3D analyses. These materials can undergo large strains with appropriate constitutive relations. In this problem, however, we employed the equivalent linear time invariant solver of `Seismo-VLAB` in 2D. Results of the viscoelastic and equivalent linear analyses are presented in the next section.

4 2D/1D Aggravation Factors: Spatial Variability

In the fourth step of the Monte Carlo simulation method, we performed finite element simulations using stochastic input parameters, both viscoelastic and equivalent linear. The element size (here, 1m x 1m) was constrained by the requirement to accurately represent the correlation structure of the stochastic field and to avoid aliasing of the minimum propagating wavelength.

100 sample functions of the stochastic field described above were generated to ensure statistically stable results, each corresponding to θ_z =9m and one of two θ_x =50m and 100m. For each realization and each horizontal correlation length, the model was subjected to 10 ground motion time series. The latter were selected by the GMC TI team as follows:

The PEER NGA-West2 database was searched for events using the criteria listed in Table 1, which yielded a total of 19 records. To provide more uniform frequency content in the records, spectral matching was performed using `RSPMatch`. The target spectrum was developed to provide a realistic input motion with suffcient high-frequency energy to identify the influence of the near-surface velocity structure. Using the [17] GMPE with model parameters $M_w = 7$; Mechanism = Normal; Dip = 60^o; V_{s30} = 1000 m/s; R_{JB}=R_{rup}=15 km; and R_x=0 km; a response spectrum for rock conditions was developed. The high frequency of the spectrum was then amplified using the [18] correction for hard-rock V_{s30} = 1600 m/s with the mean of the two models. The ensemble of spectrally matched response spectra that we used for the simulations are depicted in Figure 12.

Table 1: Search criteria used to select seed motions from NGA-West2 database

Parameter	Range
Fault type	All types
Magnitudes M_w	6.5 - 7.5
R_{JB}	0 - 30 km
R_{rup}	0 - 30 km
V	450 - 3000 m/s
D_{5-95}	20 - 100 sec

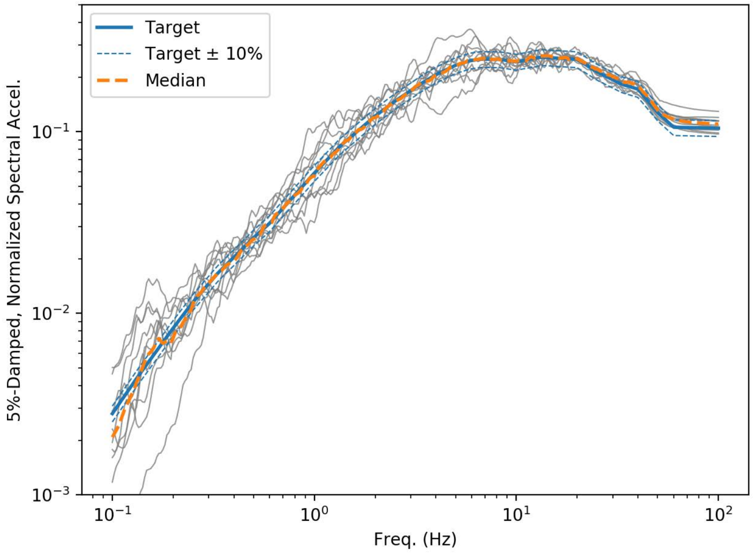

Figure 12: Matched response spectra of the selected PEER-NGA2 West database records (RSNs).

For the viscoelastic analyses, low-strain damping D_{min}=2% was included for numerical stability in the form of Rayleigh damping. For each 2D simulation (100 realizations x 2 θ_x correlation lengths), we selected 1D profiles at 15m intervals (51 profiles per model) and subjected both 2D and 1D models to each of the 10 input time series, which were prescribed as rock outcrop motions. In total, we performed 2,000 2D and 100,000 1D viscoelastic site response analyses. Figure 13 depicts one realization of the stochastic field with θ_x =50m, along with the 51 corresponding 1D profiles extracted from this realization and used to calculate the 2D/1D aggravation factors. Successively, Figure 14 depicts the surface to borehole (rigid base) amplification factor for the 1D profiles of the midpoint of each 2D stochastic field realization; as expected, the fundamental period of the site is systematically captured by the stochastic realizations, whereas the transfer functions increasingly diverge as the period decreases (frequency increases) and the wavelengths become increasingly comparable to the correlation lengths of the stochastic field.

To constrain the computational cost for the equivalent linear analyses, which involved the scaling of the above ground motion amplitudes to 0.4g, 0.55g and 0.7g, we only used three ground motions (modified_RSN289_h2-pb.acc, modified_RSN4869_h2-pb.acc, and modified_RSN164_h2-pb.acc) and verified that results were statistically stable (see Appendix to this report for more details). In total, 1,800 2D and 90,000 1D equivalent linear analyses were performed (100 realizations x 2 θ_x correlation lengths x 3 ground motions x 3 scaling amplitudes x 51 1D profiles). All simulations were performed with the fully-parallel version of `Seismo-VLAB` on the Caltech HPC cluster (`https://www.hpc.caltech.edu`).

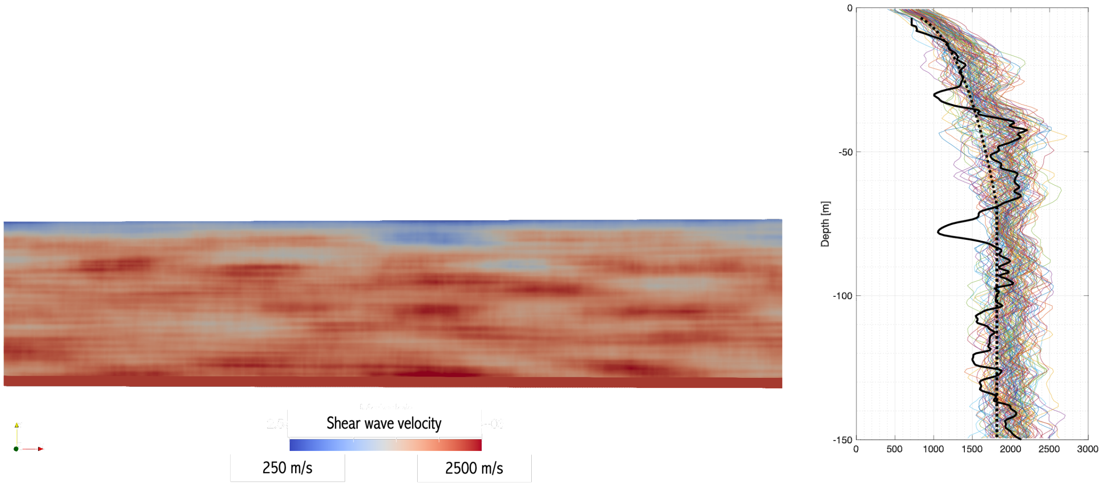

Figure 13: (top) Realization of the stochastic field with θ_x =50m mapped on the finite element mesh with element size 1m x 1m. (bottom) 51 1D profiles extracted from the 2D model for the estimation of the 2D/1D aggravation factors; as well as moving average V_s data ensemble variation with depth; and V_{sav} spatial trends used to compute the standardized V_s data.

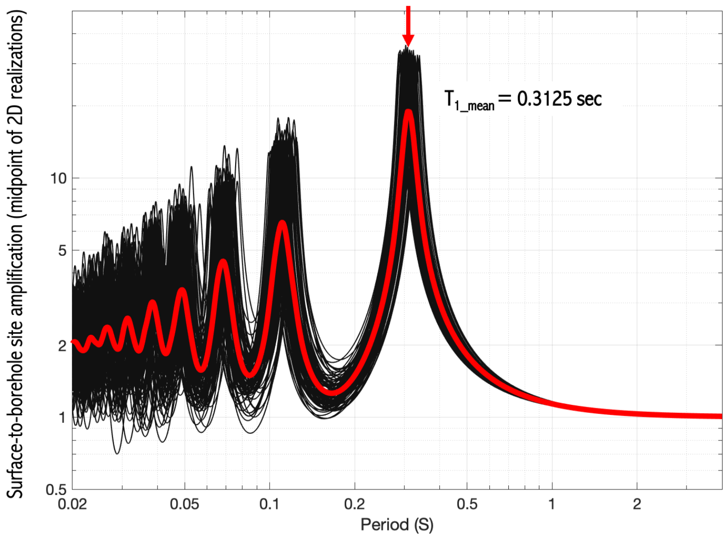

Figure 14: Surface to borehole (rigid base) amplification factor for the 1D profiles of the midpoint of each 2D stochastic field realization (here shown for θ_x =50m), showing the fundamental period of the profile to be equal to T_1=0.3125 sec.

4.1 Viscoelastic Analyses

Aggravation factors are next presented in terms of mean, 16th, 25th, 75th, 84th and 95th percentile spectral ratios; as well as in terms of standard deviation of the natural logarithm of the spectral ratio with period, for each of two horizontal correlation lengths studied, namely θ_x =50m and θ_x =100m. Aggravation factors were evaluated on the ground surface of the 2D models relative to the 1D response of: (a) the profile at the midpoint of each model; and (b) the profiles corresponding to each ground surface monitoring point on the 2D model (here, 51 1D profiles per 2D realization). Results are shown in Figure 15 for the 2D/1D factors normalized by the 1D site response of the profile corresponding to the 2D model midpoint; Figure 16 for the 2D/1D factors normalized by the 1D site response of the profiles corresponding to the monitoring points on the surface of the 2D models; and Figure 17 depicts the σ of the natural logarithm of the 2D/1D factors for each set of normalized ensembles.

As can be readily seen, the mean of the two sets of 2D/1D factors for the same correlation length (here, θ_x =50m) are nearly identical; they attain maximum aggravation of $\approx 5\%$ at period T=0.075 sec, which coincides with the length-scale of the horizontal correlation length of the random field; and become equal to 1 for periods longer than the fundamental period of the site ($\approx T$ =0.3125 sec), beyond which the propagating wavelengths are too long to be affected by the 1D site response of this particular model. The σ of the natural logarithm of the two ensembles of 2D/1D factors, which is also reflected on the SA_{2D}/SA_{1D} percentiles, is substantially different for periods shorter than the fundamental site period. After discussion with members of the GMC TI team, it was decided that –since the 2D/1D factors will be applied on the target site factors outside the logic tree– the ensemble with the lower σ would be representative of the site response aggravation due to 2D site effects, without double counting the effects of 1D randomization that will be already accounted for in the case of the site factors. In the remainder of the document, when we refer to 2D/1D aggravation factors we will imply the spectral ratios with the lower σ, used unless otherwise stated. The mean 2D/1D response spectral aggravation factor of $\approx 5\%$ is aligned with findings by [19] and others, especially if we consider the relatively short horizontal correlation length (here, θ_x =50m) compared to the propagating wavelengths (here, λ_x =100m in the top 20m at 10Hz, on average); the COV of the velocity profile statistics (0.12-0.24 in the top 60m of the profile); and the finite element mesh resolution that was not optimized to capture frequencies 20Hz or higher, where the effects would probably have been more pronounced for the idealized site and material properties used in this report.

Figure 18 next compares the σ of the natural logarithm of the response spectra ensemble of the 2D simulations recorded at 51 locations on the ground surface ($50,000$ response spectra from $1,000$ analyses); the corresponding 1D site response analyses with the same input motions corresponding to the profiles of the each receiver on the surface of the 2D profiles ($50,000$ response spectra from $50,000$ analyses); the σ of the natural logarithm of the response spectra ensemble of the 10 input motions; and the σ of the natural logarithm of the 2D/1D factors (where 2D response is normalized by the corresponding 1D response at each of 51 receiver sites per 2D model). As can be seen, the σ of the 1D and 2D response spectra are comparable and 2-5 times higher than that of the input motions for periods below the fundamental period of the site. For periods larger than T=0.3125 sec, the σ of the 2D/1D ratio plummets as previously discussed; while the σ of the 2D and 1D response spectra become identical and closely follow the σ of input ground motions which, for this period range, are not influenced by 1D or 2D site response at the site.

Lastly, Figures 19 and 20 compare the mean, $16^{th}, 25^{th}, 75^{th}, 84^{th}$ and 95^{th} percentile of 2D/1D factors; and the σ of the natural logarithm of the 2D/1D factors for the two horizontal correlation lengths studied, namely θ_x =50m and θ_x =100m. Results are very similar, suggesting that in this spatial correlation length range, 2D phenomena are comparable in intensity and frequency relative to 1D site response. In both figures, we note that 2D/1D factors corresponding to θ_x =100m peak at T=0.15 sec, again the period corresponding to wavelengths comparable to the horizontal correlation length of the random medium, and nearly twice the period where we observed peak for the 2D/1D factors in the case of θ_x =50m. For periods between T=0.15 sec and the fundamental period of the site (T=0.3125 sec), mean and σ of 2D/1D spectral ratios are the same for θ_x =50m and θ_x =100m, which can be explained since the propagating wavelengths in this period range are longer than 100m. For periods longer than T=0.3125 sec, mean 2D/1D factors become 1 and the σ thereof rapidly plummets to negligible values.

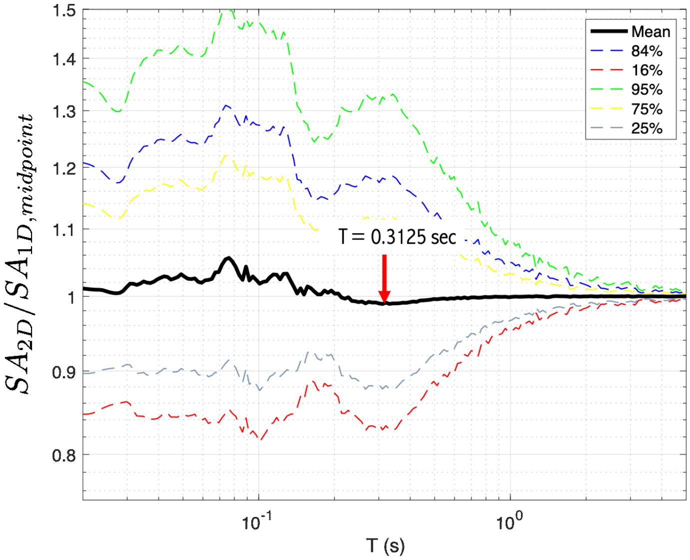

Figure 15: 2D/1D aggravation factors normalized by the 1D site response of the profile corresponding to the 2D midpoint (θ_x =50m).

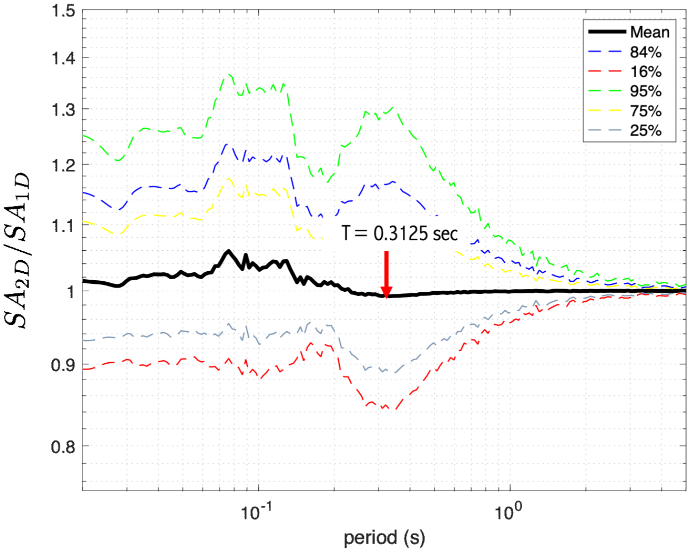

Figure 16: 2D/1D aggravation factors normalized by the 1D site response of the profiles corresponding to the monitoring points on the surface of the 2D models (θ_x =50m).

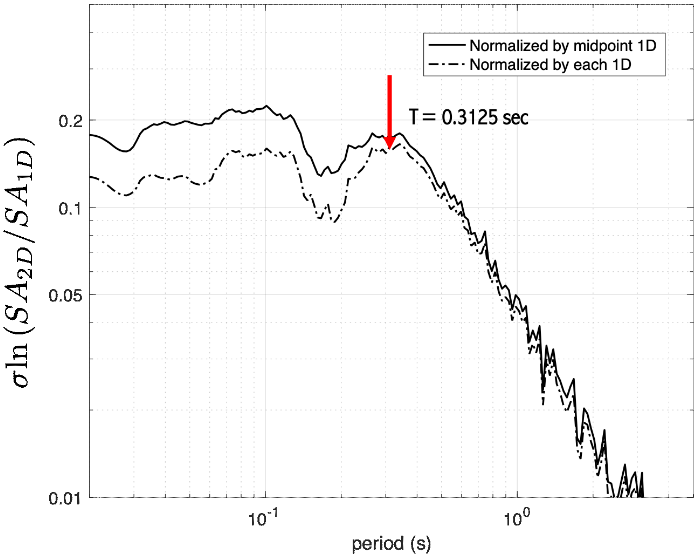

Figure 17: σ of the natural logarithm of the 2D/1D aggravation factors for each set of normalized ensembles (θ_x =50m).

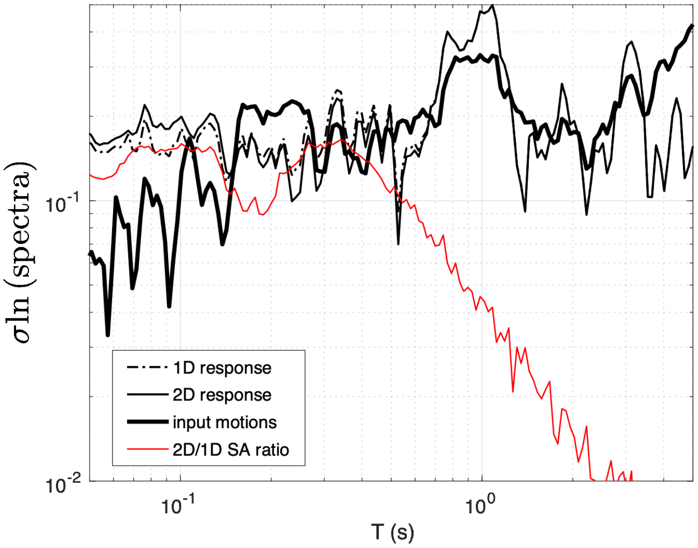

Figure 18: Comparison of σ of response spectra ensemble of the 2D, 1D simulations to the σ of the input motion response spectra and the σ of the natural logarithm of the 2D/1D factors.

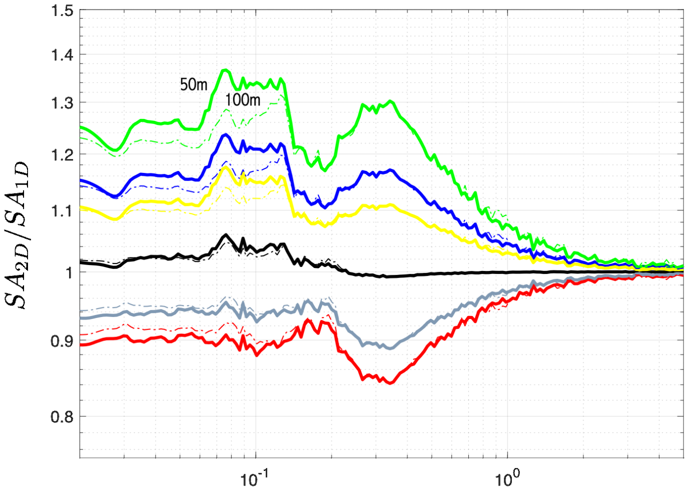

Figure 19: 2D/1D aggravation factors: Comparison of mean ratios for θ_x =50m and θ_x =100m.

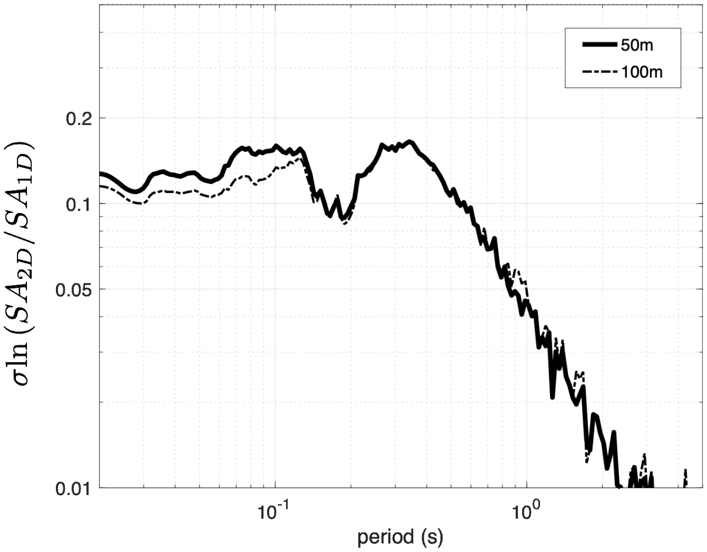

Figure 20: σ of the natural logarithm of the 2D/1D aggravation factors: Comparison of results for θ_x =50m and θ_x =100m.

4.2 Equivalent Linear Analyses

We next repeated the 2D and 1D simulations described above for the same 100 random field realizations and same 51 profiles per realization using time invariant equivalent linear analyses. To assign nonlinear dynamic properties (G/G_{max} and ξ curves vs. mean deviatoric strain, γ) we first needed to distinguish between sediment interbeds and basalt layers in each random field realization. For this purpose, we selected a velocity threshold to serve as a proxy for the sediment/basalt boundary. For elements stiffer than this threshold, we assigned basalt nonlinear dynamic properties, and for elements softer than this threshold, we assigned sediment nonlinear dynamic properties. Payne et al (2007) derived sediment and basalt velocity-depth relationships using analog data; these functions are also digitized in `AnalogVels_Sediment_Payne-et-al_2012.xlsx`. The two V_s relationships are depicted in Figure 21. After studying the resulting distribution of 1D profiles that resulted from our random field analysis, which involved data resampling, smoothing, idealized background velocity profile and COV profile trends, and truncation of the probability distribution function (PDF) between (-2 σ, 2 σ), we combined the basalt and sediment generic V_s relationships as shown in Figure 21. To constraint the threshold curve near the surface, that is heavily affected by the steep decay of the basalt V_s generic function, we established a data-driven lower bound limit for the basalt at $V_s = 650$ m/sec, as shown in Figure 21. Using this empirical threshold, sections of the V_s profiles that lie on the left of the threshold, or have $V_s \leq 650$ m/sec are assigned sediment nonlinear properties; while the rest of the profiles are assigned basalt nonlinear properties. A Python function was developed that evaluated the ensemble of 150,000 elements per 2D model against the threshold, and assigned nonlinear properties across the numerical domain for each realization.

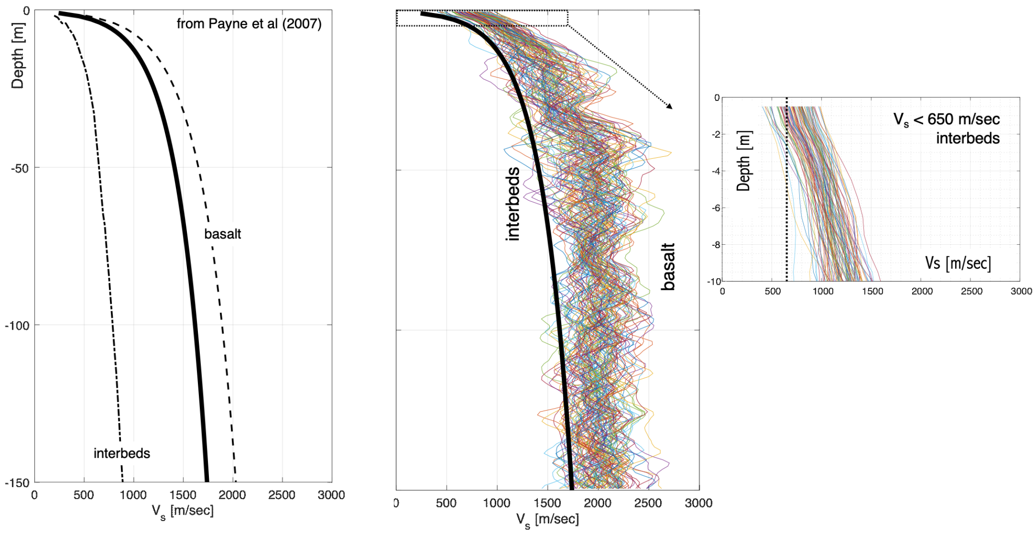

Figure 21: Basalt-sediment interbed empirical threshold based on Payne et al (2007) analog velocity-depth analog relationships.

To model the dynamic nonlinear behavior of the interbeds, we used the Menq (2003) [20] modulus-reduction and damping curves, which are a function of the coefficient of uniformity and mean effective confining pressure; we assigned C_u =10 per suggestion of the GMC TI team, and evaluated the mean effective confining pressure at the centroid of each finite element prior to assigning nonlinear properties. The modulus reduction and damping curves for three different depths in the model are shown in Figure 22. For the dynamic nonlinear behavior of the basalt, we used the North and Rizzo (2015) coefficient recommendations for basalt using the Darendeli (2001) [21] MRD model without any dependence on confining pressure. The G/G_{max} and ξ curves that were assigned uniformly to the ensemble of finite elements classified as basalt (on the basis of the empirical threshold described above) are depicted in Figure 23.

The ground motions used in the linear viscoelastic analyses were successively scaled to 0.4g, 0.55g and 0.7g amplitude. The frequency content was unaltered. Three ground motion time series (modified_RSN289_h2-pb.acc, modified_RSN4869_h2-pb.acc, and modified_RSN164 _h2-pb.acc) were selected from the ground motion ensemble of 10 time histories; each was scaled to 3 PGAs, and used as an input to 100 2D and 5,100 1D equivalent linear models. Only one correlation length θ_x =50m was used, given the negligible sensitivity of the 2D/1D factors to the correlation lengths considered in the viscoelastic analyses. The scaled ground motion time series were successively deconvolved through the 1D profile that corresponded to the midpoint of each 2D model, and the rock outcrop time series was used as stress input to the base of each model, allowing for radiation damping of the downgoing waves towards the halfspace. An example is shown in Figure 24.

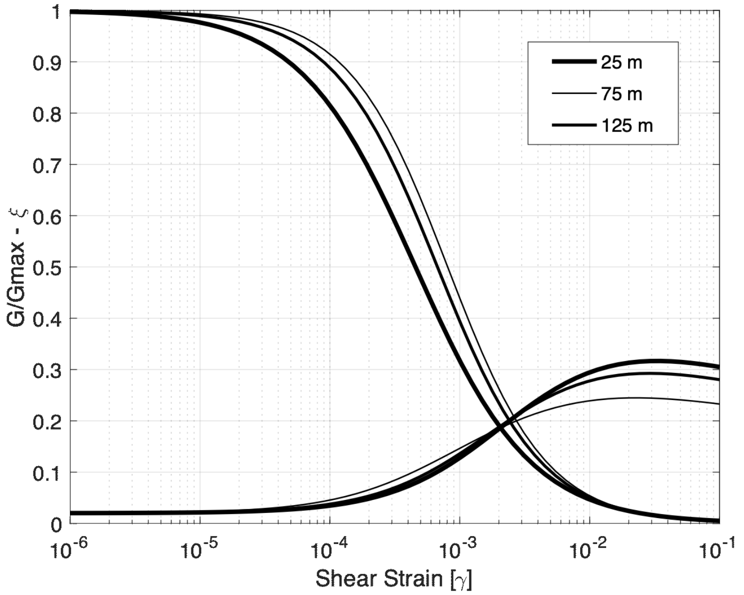

Figure 22: Menq (2003) [20] modulus-reduction and damping curves for C_u =10, evaluated at three different depths.

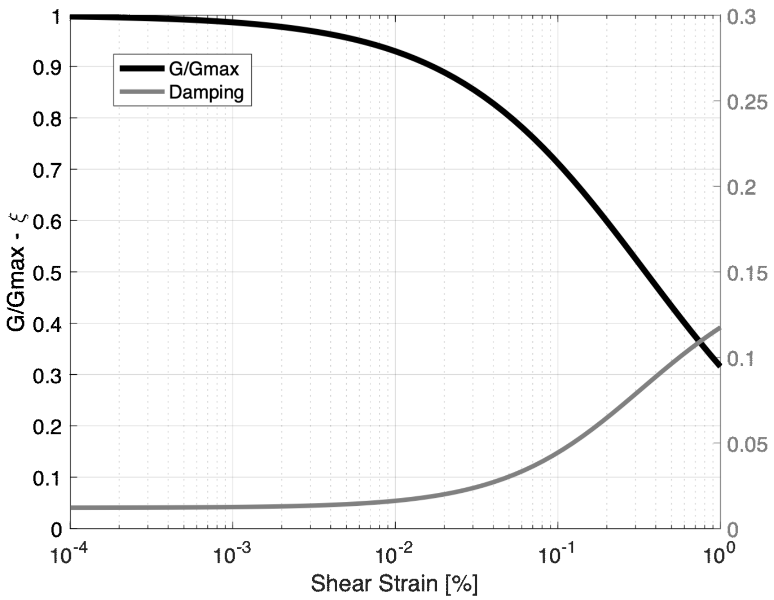

Figure 23: North and Rizzo (2015) coefficient recommendations for basalt using the Darendeli (2001) [21] MRD model without any dependence on confining pressure.

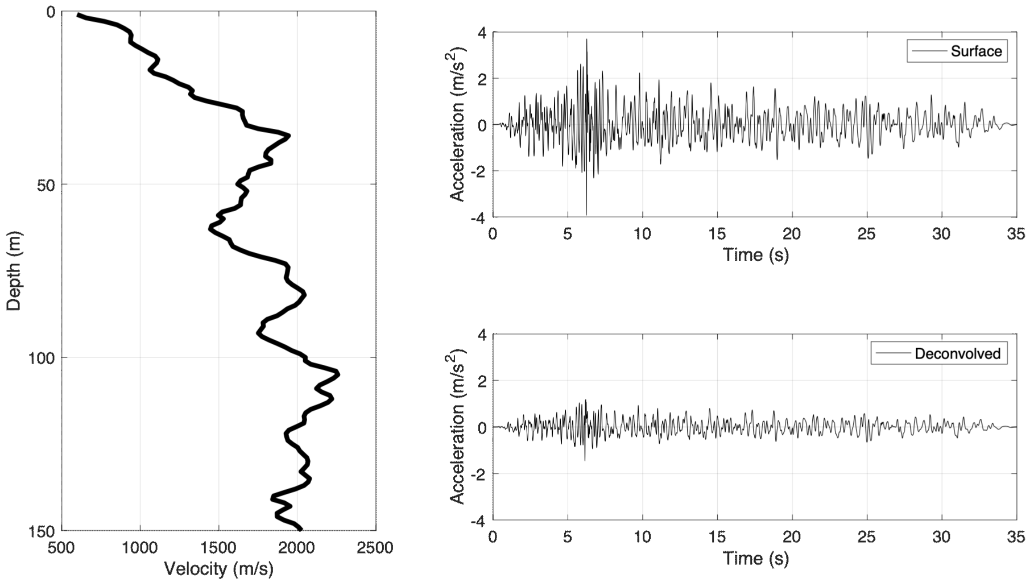

Figure 24: (left) Sample 1D profile at the midpoint of one of the 100 2D realizations of the stochastic field used for the equivalent linear analyses; (right, top) scaled ground motion time series to 0.4g; and (right, bottom) deconvolved ground motion time series to rock outcrop motion, that was successively used as input to equivalent linear analyses.

Figure 25 successively compares the mean 2D/1D factors from the equivalent linear simulations for PGA=0.7g intensity and θ_x =50m, to the corresponding values from the viscoelastic analyses. Note that since we only used 3 ground motion time series for the equivalent linear analyses, we extracted results for the same time series from our viscoelastic simulations. Results were found to be nearly identical to the viscoelastic results, both in terms of mean and percentiles, as well as in terms of σ as depicted in Figure 26.

To further analyze the reasons behind the unaltered 2D/1D factors despite the large intensity ground shaking in this case, Figure 27 plots the modulus reduction at convergence of one of the 100 2D equivalent linear analyses using the 0.7g intensity ground motion input. As can be readily seen, G/G_{max} on the order of 75% is only evident in the top 2-5m of the profile. The thickness of this layer is too small for the propagating wavelengths to be meaningfully affected by, which explains why results of the viscoelastic and the equivalent linear analyses, however strong the motion, were not affected by the nonlinear response of the soil profile.

The presence of heterogeneous soil patches on the ground surface of the soil profile also allows for larger strains to be developed compared to the horizontally stratified infinitely wide 1D models. Results are shown in Figure 28, where the top 5m of the strain profile distribution corresponding to the 2D simulation of Figure 27 has systematically larger strains compared to the 1D equivalent linear analyses using the same input motion. Nonetheless, the 2D and 1D strain profiles converge for depths more than 5m, namely for the sections of the profile that are meaningfully affected by site response in the frequency range $\leq$ 20 Hz. This relationship between 1D and 2D deviatoric strains at various depths for the ensemble of 2D simulations for 0.7g is confirmed in Figure 29; the left hand side plots the relationship between 1D and 2D simulations at 2m depth; while the right hand side plots the same relationship for 5, 10 and 15m. Overall, the scatter of the plot at 2m depth is larger and the 2D strains are systematically higher than the 1D strains at the same depth, whereas at the deeper sections of the profiles, 1D and 2D strains plot along a 1:1 relationship.

On the same time, looking more closely at the strain distribution at 15m depth, Figure 30 separates the basalt and sediment interbed elements at depth 15m for the 0.7g input motion simulations: as can be seen, the sediment element 1D strains are on average larger at the corresponding 2D strains, by contrast to the nearly 1:1 distribution of the basalt elements. This difference is attributed to the nature of 1D site response simulations, where softer sediment interbed elements are not surrounded by stiffer basalt elements, and are thus subjected to larger strains than the corresponding elements in the 2D models.

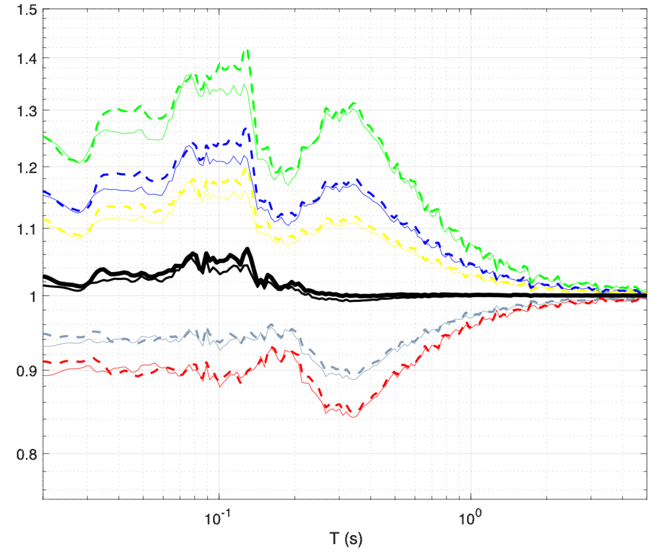

Figure 25: Mean 2D/1D factors from the equivalent linear simulations for PGA=0.7g intensity and θ_x =50m: thin lines (viscoelastic); and dashed thick lines (equivalent linear).

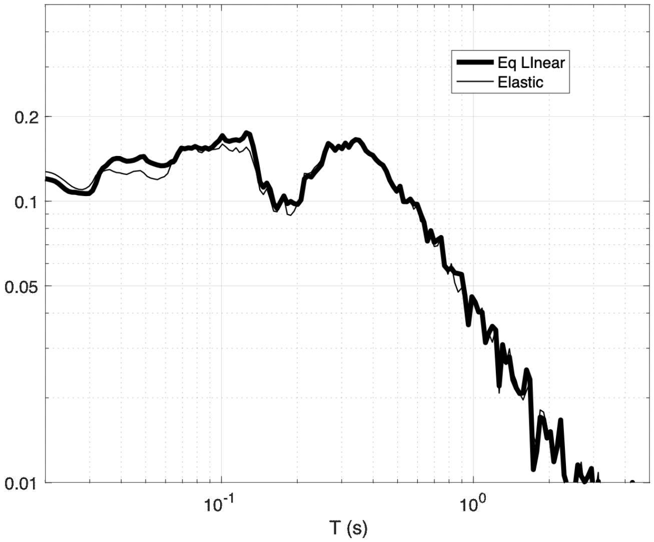

Figure 26: Comparison of σ of natural logarithm of 2D/1D factors between the viscoelastic and the equivalent linear simulations for PGA=0.7g intensity and θ_x =50m.

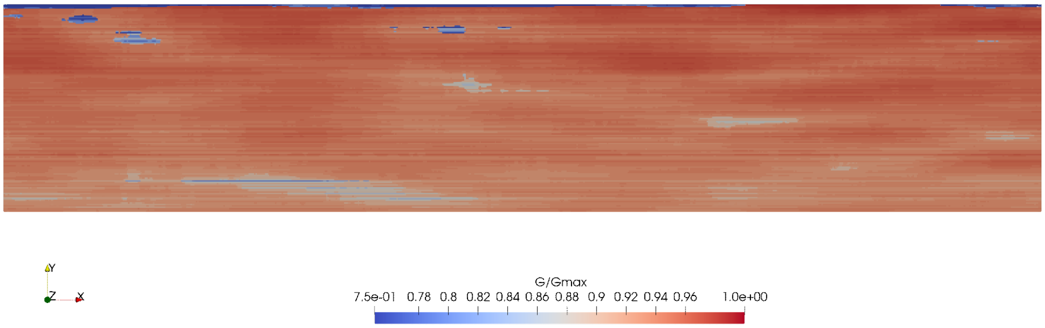

Figure 27: Modulus reduction (G/G_{max} at convergence of one of the 100 2D equivalent linear analyses using the 0.7g intensity ground motion input.

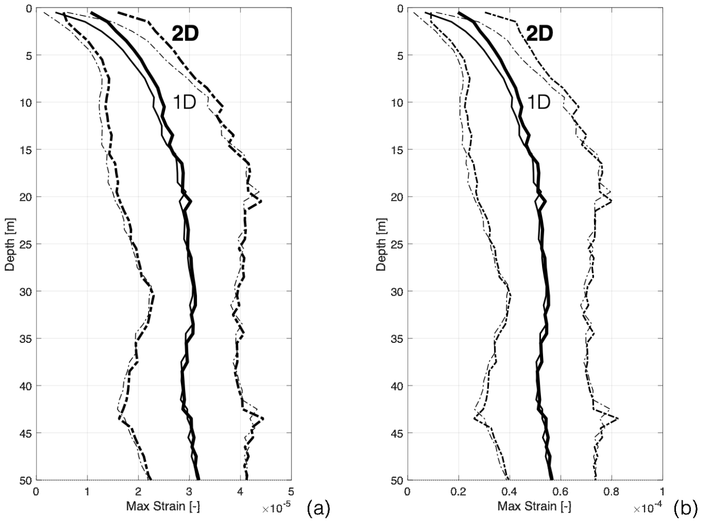

Figure 28: Mean and standard deviation of 1D and 2D deviatoric strain profiles for 0.4g equivalent linear simulations (left) and 0.7g equivalent linear simulations (right).

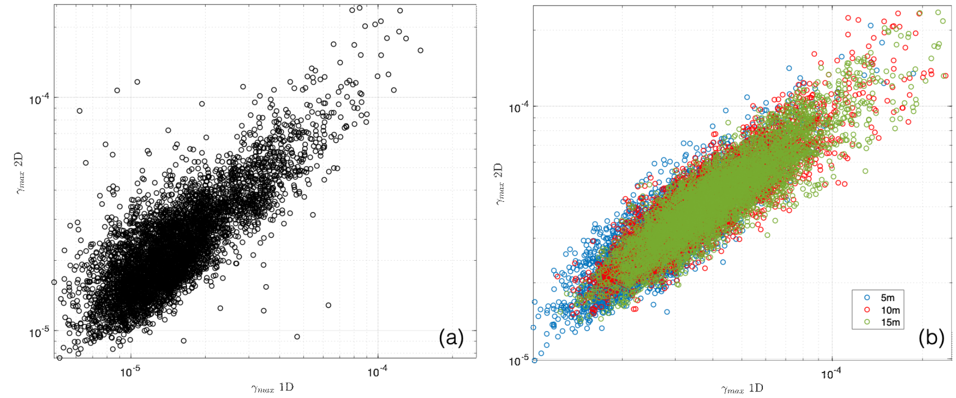

Figure 29: (left) Relationship between 1D and 2D simulations at 2m depth for the ensemble of 2D simulations for 0.7g; (right) same relationship for 5, 10 and 15m.

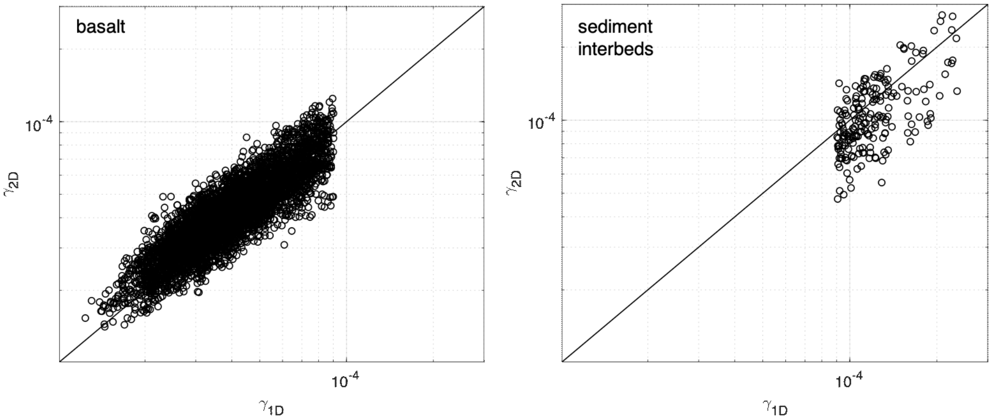

Figure 30: (top) Relationship between 1D and 2D simulations at 15m depth for the ensemble of 2D simulations for 0.7g, separately plotted for basalt and sediment interbed elements. The straight line corresponds to 1:1 relationship, suggesting that the sediment interbed sediments in 1D are subjected to larger strains that the corresponding elements in the 2D models, where they are surrounded by stiffer basalt elements that constrain the strain amplitude at a given depth, on average.

5 2D/1D Aggravation Factors: Edge Effects

In the second phase of the project, we quantified the corner effects of the Eastern Snake River Plain subsurface geometry in the vicinity of Site 3 by developing a 2D cross section idealized model of the site, and subjecting it to vertically propagating in-plane shear waves and a range of inclined plane shear waves consistent with the seismotectonic setting of the area. To develop the 2D idealized cross-section, we relied heavily on the literature, and in particular on McCurry et al [22] and Twining et al [23] who developed models of the subsurface that synthesize existing geologic, deep-borehole, and geophysical data in the vicinity of Site 3.

5.1 Numerical Model Development of the Eastern Snake River Plain Edge

Site 3 lies within INL's Geothermal Resource Research Area (GRRA) in the Eastern Snake River Plane (ESRP). The GRRA sits on the northern margin of the ESRP and is located in a geological region that is dominated by the Yellowstone volcanic track and underlain by several hundred meters of interbedded Pleistocene basalt lavas erupted from widely scattered vents on the ESRP and sediment derived from mountain ranges northwest of the plain. Several boreholes penetrate through the entire basalt section in the GRRA and INL area, INEL-1 (to 3.16 km), WO-2 (to 1.52 km), 2- 2A (to 910 m), and most recently USGS 142 (to 573 m) (see Figure 31). Figure 32 illustrates a northwest-southeast cross-section of the GRRA and surroundings [22].

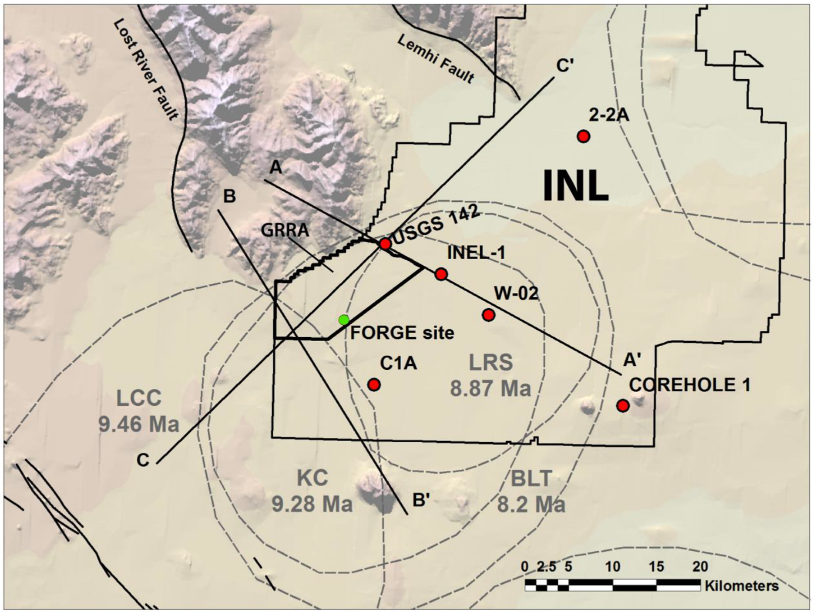

Figure 31: Regional map showing the INL, GRRA, caldera boundaries, and deep boreholes. Inferred caldera boundaries are shown as dashed lines (LCC – Little Choke Cherry; KC – Kyle Canyon; LRS – Little Lost River; BLT – Big Lost Trough). Locations of the LCC, KC, and LRS caldera boundaries are from Anders et al. [24], and the BLT boundary is from McCurry et al. [22]. Location of cross-section A-A' (Figure 31) are also indicated.

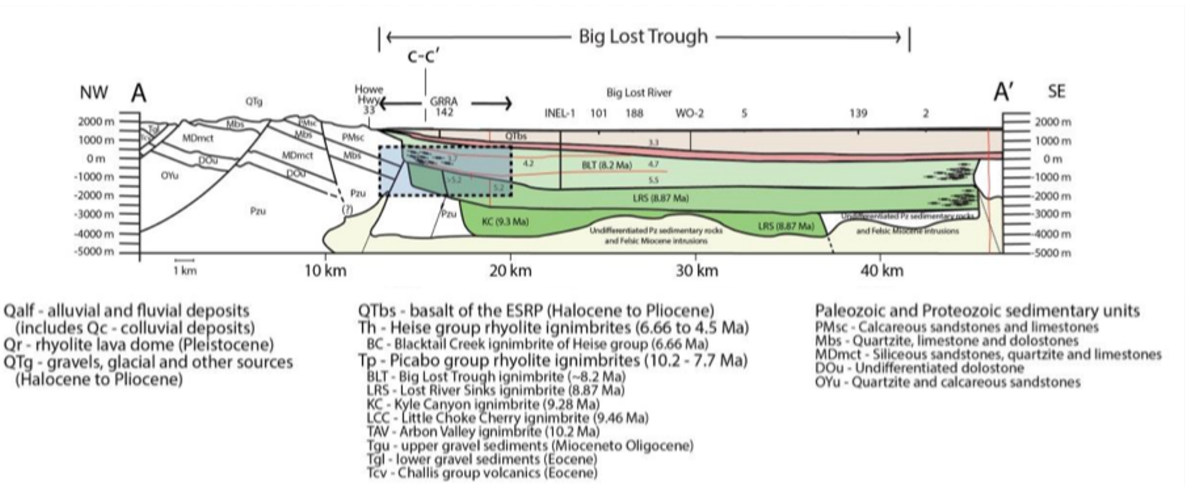

Figure 32: Cross-section A-A' after McCurry et al. [22]. Cross-section locations are shown in Figure 30. Thin red lines in AA' show the Pankratz and Ackerman [25] velocity model. Blue shaded region indicates extent of GRRA at a depth of 1.5 to 4 km (4,900 to 13,000 ft).

Seismic refraction and electrical resistivity surveys traversing the GRRA identify a steeply dipping structure separating the SRP from the sedimentary rocks to the north (Figure 32, after [25]). Cross-section AA', which extends from the Arco Hills to the southeast across the center of GRRA and roughly parallels the seismic survey line of Pankratz and Ackermann [25] formed the basis of our numerical model, shown in Figure 33. The cross section is quite well constrained, since it crosses close to three deep boreholes (USGS 142; INEL-1; and WO-2). Faint red lines and red numbers illustrate the velocity model boundaries and modeled seismic velocities of Pankratz and Ackerman [25] which consisted of six layers. Velocities were found to increase in the basaltic rocks from 1.5 km/s at the ground surface to 3.3 km/s at a depth of approximately 200 m. Lateral variability was observed within the rhyolite ignimbrites (denoted Tp2 in Figure 32). Deeper layers were not modeled in detail given the relatively high frequency range where our study concentrated (0.2-5 Hz).

Viscoelastic simulations were performed with the 64-bit parallel processing version of FLAC2D (`www.itascacg.com/software/flac`). A finite difference code, such as FLAC, was chosen to accommodate the $\approx 20M$ elements of this model; a spectral element code (such as SPECFEM2D) would have also been efficient in this case, as would have been an e-tree finite element-based code like Hercules. The model was developed, tested and locally refined to ensure that is was aliasing-free in the target frequency range (0.2-5 Hz). The model dimensions, including halfspace that we used to kinematically constraint the inclined wave incidence was 30km wide x 5 km depth. To capture the target frequency upper bound, the approximate size of the models was 20M elements.

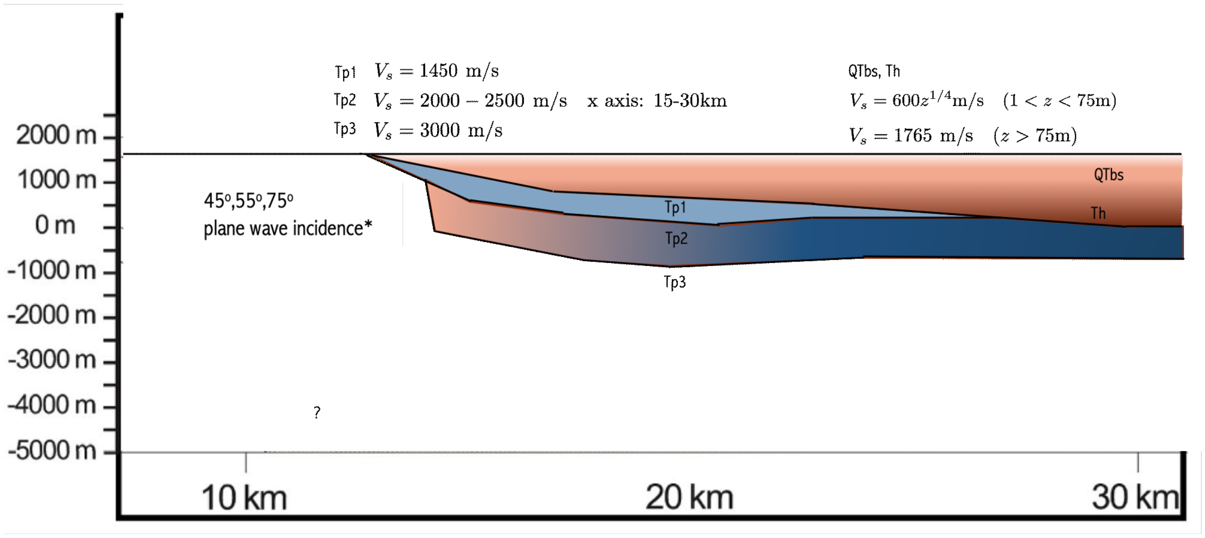

*from Table 8-7. Parameters for the thirteen regional normal fault sources, dip for Big Lost River Fault, INL SSHAC Level 1: PSHA, September 2016

nu = 0.30

Figure 33: Idealized shear wave velocity model after cross-section A-A' in Appendix A, McCurry et al. [22].

5.2 Vertical and Inclined Viscoelastic Simulations

We next used the configuration of subsurface geometry and properties in Figure 33 to perform a series of plane wave 2D analyses for a range of incidence angles constrained in part by the geometry of the normal faults on the west of the river plain, and informed by the Seismic Source Characterization (SCC) logic tree parameters for the Big Lost River Fault dip [26]. As input motion, we used a Ricker wavelet with central frequency 3.5Hz, which provided adequate energy in the frequency target range $[0.5 - 10]$ Hz of excitation. For each of the vertically incident, and three inclined input simulations (45^o, 55^o and 75^o), horizontal and vertical ground motion response spectra on the model ground surface were normalized by the 1D site response at each receiver. Figures 34 plot the horizontal acceleration seismogram synthetics of the surface ground motion for the aforementioned simulations. The maximum amplitude of horizontal motion in the vicinity of the Site 3 is shown to result from inclined wave incidence 55^o, which also persists for several km beyond the edge where it is generated. Note however that this is clearly a surface wave generated from the basin edge, and therefore is likely rich in long period motions and weak in high frequencies. Also note the lack of horizontal motion for the idealized plane wave incidence 45^o between X=0-5 km. This is the result of the analytical solution of 45^o incidence on halfspace whose stress-free boundary conditions yield a vertical amplitude response and no horizontal response on the surface. For reference, Site 3 is located at coordinate $x = 8.5$ km while the point of max horizontal response amplification is at coordinate $x = 7.25$ km.

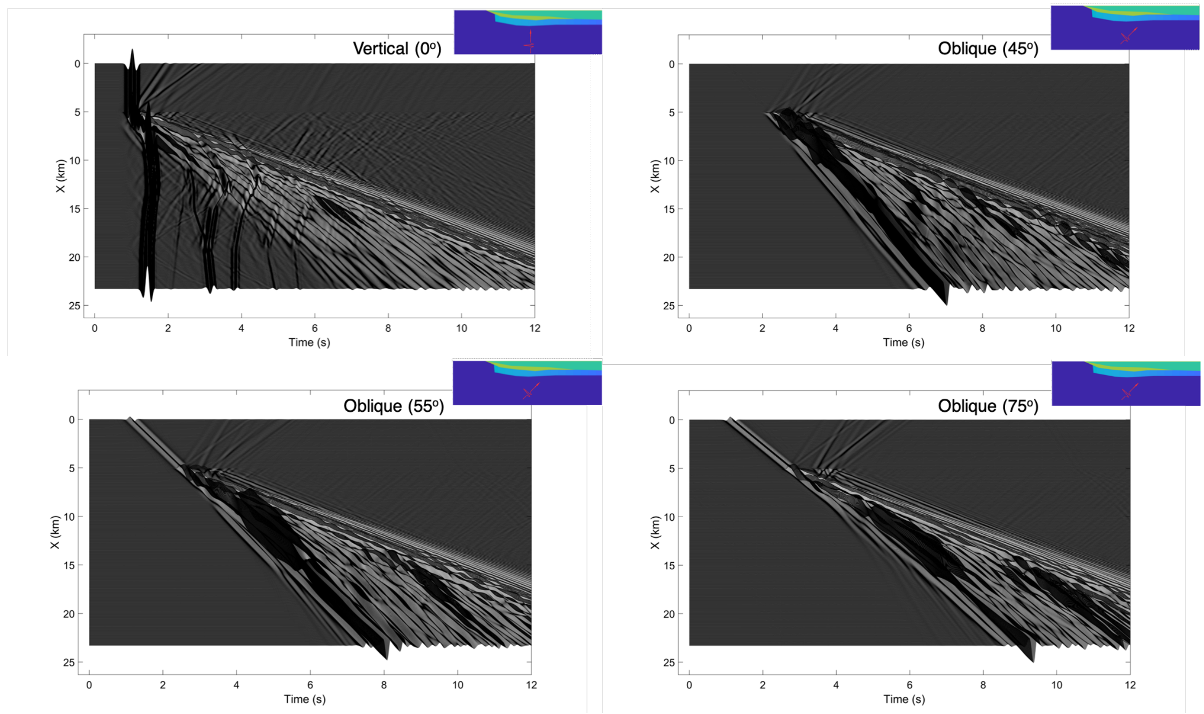

Figure 34: Horizontal acceleration seismogram synthetics of the surface ground motion for vertically incident, and three inclined input simulations (45^o, 55^o and 75^o) on the idealized edge model.

For the 55^o inclined incidence, Figure 35 depicts a snapshop of the displacement vector field, that shows the complex reflected and refracted wavefield in the vicinity of the edge, as well as two sets of Rayleigh waves traveling away from the edge, recognizeable by their characteristic retrograde particle motion.

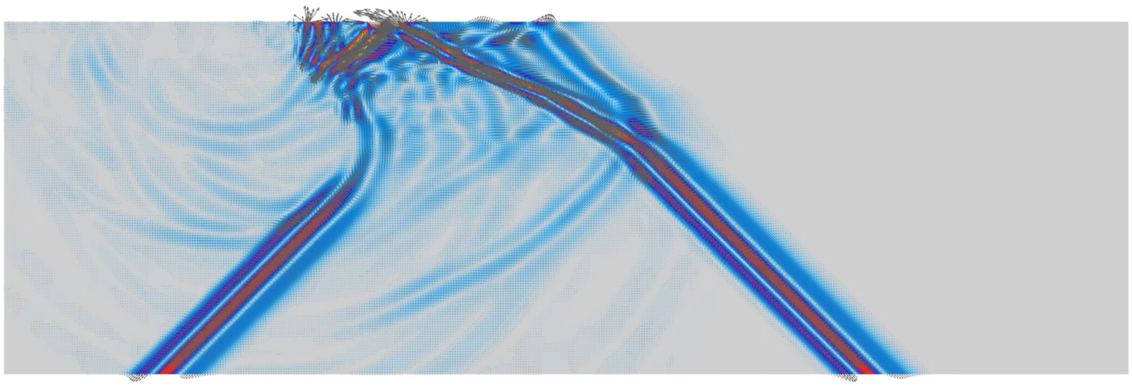

Figure 35: Displacement vector snapshot for inclined input simulation 55^o on the idealized edge model.

Lastly, Figures 36 and 37 depict the color contours of response spectral acceleration between 0.05 and 2 sec, computed at each receiver site (every 10 m) on the ground surface and normalized by the corresponding response spectral acceleration at the same site, assuming 1D site response. The dashed line in each figure denotes the edge of the sedimentary deposits, therefore from X=0-5 km, we expect to see very little if any diffracted (cylindrical) wave propagation. For example, the ratio of the vertically propagating input motion in Figure 36 is SA_{2D}/SA_{1D}=1 between 0-5 km for the horizontal motion (that is, the motion is the same as if the response at each receiver were 1D) and SA_{2D}/SA_{1D}=0 for the vertical component, since there is no parasitic vertical component for horizontally polarized incidence in the halfspace part of the model. For this same simulation, the peak horizontal response relative to 1D analyses appears at period T=0.2 sec near the USGS Site 142, $SA_{2D}/SA_{1D} \approx 1.8$.

For clarity, Figure 38 depicts the response spectra of the horizontal acceleration time series for the ensemble of 2D simulations we performed, at USGS site 142 as well as at the location where the maximum SA_{2D}/SA_{1D} is observed in the case of vertical incidence, at approximately 2.25 km from the edge of the formation. As can be seen, at site 142 1D and vertical 2D incidence analyses yield nearly the same spectra acceleration, and so does the ground response to the 45^o inclined incidence, but for a narrow period range centered around 2sec. The horizontal acceleration response to the 55^o and 75^o inclined incidence is much weaker as evidenced in the figure, but recall that the vertical (parasitic) components of motion are proportionately larger.

Similar observations one can make for the inclined incidence simulations in Figure 37. Amplification for X≥5 km is observed for the horizontal component relative to the vertically propagating 1D idealization, particularly close to the edge. All the amplification is concentrated in periods T≤1.2 sec and, based on the seismogram synthetics in Figures 34, is generated by diffraction near the edge. The vertical component is perhaps more interesting in that sense since it is shown to attain spectral amplitudes nearly as large as the horizontal spectral acceleration that would have been predicted for 1D site response near the edge. This finding is relevant to the selection of V/H factors assigned to estimate vertical ground motion amplitude from 1D site response analyses near Site 3.

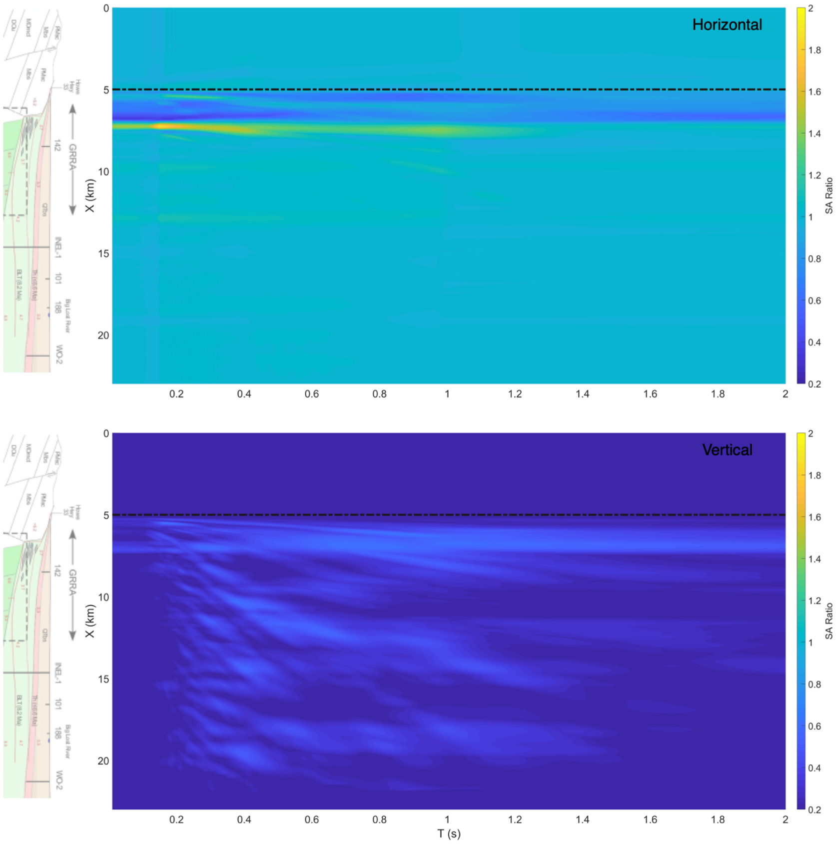

Figure 36: Color contours of response spectral acceleration between 0.05 and 2 sec, computed at each receiver site (every 10 m) on the ground surface and normalized by the corresponding response spectral acceleration at the same site, assuming 1D site response: vertical incidence.

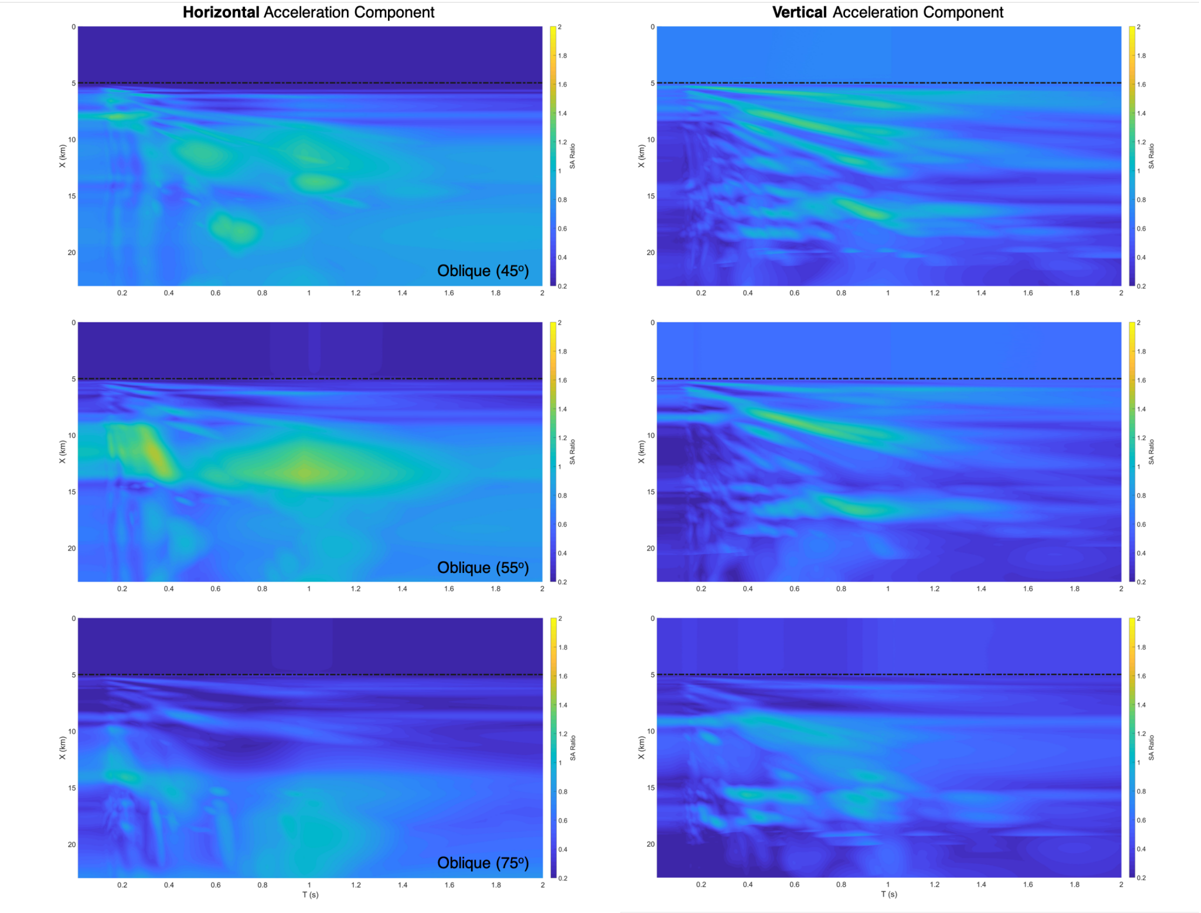

Figure 37: Color contours of response spectral acceleration between 0.05 and 2 sec, computed at each receiver site (every 10 m) on the ground surface and normalized by the corresponding response spectral acceleration at the same site, assuming 1D site response: inclined incidence.

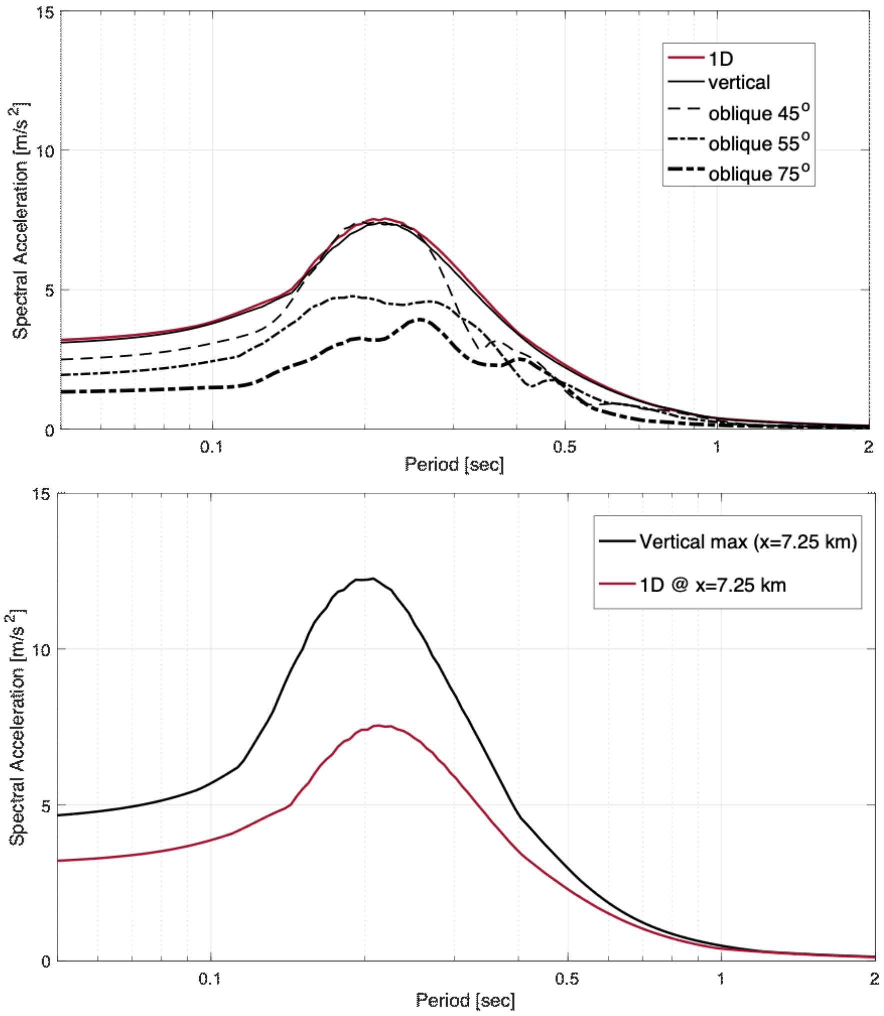

Figure 38: Response spectra (top) of horizontal acceleration time series at USGS site 142 for the ensemble of simulations we ran, including the 1D response of the profile to a Ricker pulse of central frequency 3.5Hz; (bottom) horizontal accelearion time series at distance 7.25km from the model left side (2.25km from the edge of the river deposits), where the amplitude of the response spectra for the vertical incidence is maximum, $SA_{2D}/SA_{1D} \approx 1.8.$ at T=0.2 sec.

Lastly, one could potentially challenge the dependency of the amplification patterns in Figures 36 and 37 on the basin edge *sharp corners* that were assigned to the idealized numerical model, for lack of a more detailed subsurface model. Results to that end should be interpreted in the context of wavelength filtering: a narrow band of high frequencies will indeed be affected by the sharp corners, and the same thing would hold for any smoothing one would choose to model the cross section in hand: the radius of smoothing would affect the corresponding wavelengths and bias the results accordingly. On the other side, however, the effect of the sharp geometry features of the edge effects model is of a very narrow band nature, and using a triangular averaging window across the width of the model should minimize biases associated with the said corner geometries. Of course, better subsurface geometry and stratigraphy, and 3D models could improve our 2D/1D aggravation factor estimation.

References

[1] S.J. Payne, B.D. Coryell, and J.M. Hubbell. Evaluations of existing subsurface data and recommendations for new data collection in support of inl probabilistic seismic hazard analyses. Technical Report Battelle Energy Alliance External Report INL/LTD-12-26965, Revision 0, 2012.

[2] Radu Popescu. *Stochastic variability of soil properties: data analysis, digital simulation, effects on system behavior.* PhD thesis, 1995.

[3] E Vanmarcke. Random fields: Analysis and synthesis. *Cambridge*, 1983.

[4] M Shinozuka and G Deodatis. Response variability of stochastic finite element systems. *Journal of Engineering Mechanics*, 114(3):499–519, 1988.

[5] R-S Wu and Keiiti Aki. Scattering characteristics of elastic waves by an elastic heterogeneity. *Geophysics*, 50(4):582–595, 1985.

[6] Arthur Frankel and Robert W Clayton. Finite difference simulations of seismic scattering: Implications for the propagation of short-period seismic waves in the crust and models of crustal heterogeneity. *Journal of Geophysical Research: Solid Earth*, 91(B6):6465–6489, 1986.

[7] Armen Der Kiureghian and Jyh-Bin Ke. The stochastic finite element method in structural reliability. *Probabilistic engineering mechanics*, 3(2):83–91, 1988.

[8] Bjarne Stroustrup. *The C++ Programming Language.* Addison-Wesley Professional, 4th edition, 2013.

[9] Lyndon Clarke, Ian Glendinning, and Rolf Hempel. The mpi message passing interface standard. In Karsten M. Decker and René M. Rehmann, editors, *Programming Environments for Massively Parallel Distributed Systems*, pages 213–218, Basel, 1994. Birkhäuser Basel.

[10] Leonardo Dagum and Ramesh Menon. Openmp: An industry-standard api for shared-memory programming. *IEEE Comput. Sci. Eng.*, 5(1):46–55, January 1998.

[11] George Karypis and Vipin Kumar. Metis – unstructured graph partitioning and sparse matrix ordering system, version 2.0. Technical report, University of Minnesota, Department of Computer Science & Engineering, 1995.

[12] S Kucukcoban and LF Kallivokas. A symmetric hybrid formulation for transient wave simulations in pml-truncated heterogeneous media. *Wave Motion*, 50(1):57–79, 2013.

[13] Arash Fathi, Babak Poursartip, and Loukas F. Kallivokas. Time-domain hybrid formulations for wave simulations in three-dimensional pml-truncated heterogeneous media. *International Journal for Numerical Methods in Engineering*, 101(3):165–198, 2015.

[14] Jacobo Bielak, Kostas Loukakis, Yoshiaki Hisada, and Chiaki Yoshimura. Domain Reduction Method for Three-Dimensional Earthquake Modeling in Localized Regions, Part I: Theory. *Bulletin of the Seismological Society of America*, 93(2):817–824, 04 2003.

[15] S. Kucukcoban and L.F. Kallivokas. Mixed perfectly-matched-layers for direct transient analysis in 2d elastic heterogeneous media. *Computer Methods in Applied Mechanics and Engineering*, 200(1):57 – 76, 2011.

[16] Chiaki Yoshimura, Jacobo Bielak, Yoshiaki Hisada, and Antonio Fernández. Domain Reduction Method for Three-Dimensional Earthquake Modeling in Localized Regions, Part II: Verification and Applications. *Bulletin of the Seismological Society of America*, 93(2):825–841, 04 2003.

[17] Brian S-J Chiou and Robert R Youngs. Update of the chiou and youngs nga model for the average horizontal component of peak ground motion and response spectra. *Earthquake Spectra*, 30(3):1117–1153, 2014.

[18] Olga-Joan Ktenidou and Norman A Abrahamson. Empirical estimation of high-frequency ground motion on hard rock. *Seismological Research Letters*, 87(6):1465–1478, 2016.

[19] E El Habar, C Cornou, D Jongmans, D.Y Abdelmassih, and F Lopez-Caballero. Influence of 2D heterogeneous elastic soil properties on surface ground motion spatial variability. *Soil Dynamics and Earthquake Engineering*, 123(1):75–90, 2019.

[20] Farn-Yuh Menq. *Dynamic properties of sandy and gravelly soils*. PhD thesis, 2003.

[21] Mehmet Baris Darendeli. *Development of a new family of normalized modulus reduction and material damping curves*. PhD thesis, 2001.

[22] Michael McCurry, Travis McLing, Richard P Smith, William R Hackett, Ryan Goldsby, William Lochridge, Robert Podgorney, Thomas Wood, David Pearson, John Welhan, et al. Geologic setting of the idaho national laboratory geothermal resource research area. In *Proceedings, 41st Workshop on Geothermal Reservoir Engineering: Stanford University, Stanford California, SGP-TR-209*, 2016.

[23] Brian V Twining, Mary KV Hodges, Kyle Schusler, and Christopher Mudge. Drilling, construction, geophysical log data, and lithologic log for boreholes usgs 142 and usgs 142a, idaho national laboratory, idaho. Technical report, US Geological Survey, 2017.

[24] Mark H Anders, David W Rodgers, Sidney R Hemming, Janet Saltzman, Victor J DiVenere, Jonathan T Hagstrum, Glenn F Embree, and Robert C Walter. A fixed sublithospheric source for the late neogene track of the yellowstone hotspot: Implications of the heise and picabo volcanic fields. *Journal of Geophysical Research: Solid Earth*, 119(4):2871–2906, 2014.

[25] Leroy W Pankratz and Hans D Ackermann. Structure along the northwest edge of the snake river plain interpreted from seismic refraction. *Journal of Geophysical Research: Solid Earth*, 87(B4):2676–2682, 1982.

[26] Suzette J. Payne, Ryan Coppersmith, Kevin Coppersmith, Adrian Rodriguez-Marek, Valentina Montaldo Falero, and Robert Youngs. SSHAC level 1 probabilistic seismic hazard analysis for the idaho national laboratory. Technical Report Battelle Energy Alliance External Report INL/EXT-15-36682, Revision 2, 2016.